Journal of
Materials Chemistry A
Materials for energy and sustainability

This article can be cited before page numbers have been issued, to do this please use: A. A. Eissa, N. H. Kim and J. H. Lee, *J. Mater. Chem. A*, 2020, DOI: 10.1039/D0TA06987F.

Article type: Full Paper

View Article Online
DOI: 10.1039/D0TA06987F

Rational Design of Highly Mesoporous Fe–N–C/Fe_3C/C–S–C Nanohybrid with Dense Active Sites for Superb Electrocatalysis of Oxygen Reduction

Ahmed Al-Shahat Eissa,[ab] Nam Hoon Kim[a]*, Joong Hee Lee[ac]*

[a]Department of Nano Convergence Engineering, Jeonbuk National University, Jeonju, Jeonbuk 54896, Republic of Korea. E-mail

[b]Department of Chemistry, School of Science, South Valley University, Qena, 83523, Egypt

[c]Carbon Composite Research Center, Department of Polymer-Nano Science and Technology, Jeonbuk National University, Jeonju, Jeonbuk 54896, Republic of Korea
*Corresponding Author: nhk@jbnu.ac.kr(Prof N.H. Kim), jhl@jbnu.ac.kr(Prof J.H. Lee)

Abstract

Innovating efficient and robust electrocatalysts with economic production cost for the oxygen reduction reaction (ORR) is of utmost significance for enhancing the energy efficiency of fuel cells and metal-air batteries. Herein, a single-step doping/annealing strategy has been developed for fabricating Fe–N–C/Fe_3C/C–S–C nanohybrid with high N-doping level, well-defined mesoporous/microporous architecture, and high density of efficient active sites. The importance of tuning the S-doping into the electrocatalyst carbon framework has been fully elaborated for the first time. Under the alkaline conditions, the nanohybrid displayed exceptional onset potential (E_0) and half-wave potential ($E_{1/2}$) of 1.078 and 0.929 V vs reversible hydrogen electrode (RHE). Furthermore, it manifests dominant four-electron transfer reaction, marvelous selectivity for the ORR in the presence of methanol, and excellent durability after 15,000 potential cycles with almost zero disintegration in performance under both acidic and alkaline conditions. The superb performance is due to the high density of active sites that efficiently catalyze the ORR, like FeN_x, FeS_x, Fe_3C, pyridinic–N, graphitic–N, C–S–C, and C–SO_x–C. In addition, the high graphitization degree boosts the electron conductivity and corrosion resistance; meanwhile, the high surface area and ideal mesoporosity enhance the mass transfer and facilitate the maximum exposure of the active sites to the electrolyte and reactants.

Keywords

core-shell nanostructure, oxygen reduction reaction, durability, Fe–N–C/Fe_3C/C–S–C nanohybrid, graphitic carbon

1. Introduction

The explosive growth of the worldwide population and rapid advancement of modern society have caused serious problems, such as the impairment of the ecological environment and the drastic deficiency of fossil fuels.[1] In this regard, exploring clean and sustainable energy sources is of great importance. Fuel cells are one of the greenest energy technologies that generate clean, sustainable, and efficient energy that can be utilized for future portable electronic devices and transportation systems.[2,3] Unfortunately, the sluggish ORR kinetics occurring on the cathodic part of the fuel cell-based devices restrict the overall device performance. This sluggishness can be compensated by using high platinum (Pt) loadings on the cathode. Nevertheless, the high-cost, scarcity, and poor long-term stability of Pt preclude the widespread commercialization of fuel cell-based devices.[4,5] Hence, the development of alternative ORR electrocatalysts with largely minimized cost and competitive performance is highly desirable. Several groups have developed different kinds of nonprecious catalysts for promoting the ORR. Wei Xia et al.[6] fabricated ultrathin N-doped graphene nanomesh by efficient strategy. The catalyst displayed remarkable activity towards the ORR in acidic medium. Ultrafine molybdenum carbide NPs supported on N-doped carbon nanosheets showed high performance for catalyzing the ORR in basic electrolyte.[7] Nitrogen-coordinated iron atoms supported on carbon (Fe–N–C) are the most promising non-precious ORR electrocatalysts,[8-11] since they exhibited remarkable activity compared to the Pt-based electrocatalysts,[12] due to the robust interaction between Fe and N moieties in the carbon matrix, which promotes the O_2 adsorption and accelerates the shattering of O–O bond.[13] Notwithstanding the considerable effort devoted for the design of Fe–N–C electrocatalysts, there are still some bottlenecks. For example, most of the synthetic methods for preparing the Fe–N–C electrocatalysts are solution-based strategies which are laborious, where many arduous steps are involved, such as acid washing,[14,15] removal of template,[16] and post-treatment with ammonia.[17] These conventional protocols produce ecologically deleterious waste and consume time, energy and material. The huge quantities of waste produced as a result of utilizing solvents throughout the fabrication protocols harmfully influence on the environment and public health. Consequently, there is imperious demand for cleaner, safer, and more sustainable chemical syntheses, specially the raw materials are becoming scarcer.[18]

In addition, the Fe–N–C electrocatalysts still suffer from insufficient performance, because of the restricted number of active sites, low porosity, and inadequate stability.[19,20] The deficiency in the number of active sites can be compensated by increasing the catalyst loading; however, this way results in increasing the thickness of catalyst layer, and hence increasing the mass-transfer resistance. It is noteworthy to clarify that not all the active sites participate in the ORR activity, due to their different locations in the carbon matrix. The active sites exist nearby the external surface of the material contribute easily in the ORR, meanwhile those are deeply present in the carbon matrix remain inactive. Enhancing the external surface area and mesoporosity is an efficient route to solve this problem, where the mesopores construct channels to the inaccessible active sites, and hence improve the utilization of the active sites.[21] Inspired by this, we not only aim to increase the density of active sites, but also to maximize their utilization as real active sites, by promoting the external surface area and mesoporosity to achieve the ultimate exposure of the active sites to the reactants and boost the mass transfer during the ORR process. It is noteworthy that the application of mesoporous materials not only limited to the catalytic field but also includes diverse applications. For example, mesoporous silica NPs have many applications in biomedicine, such as tissue engineering, biosensing, and drug/protein/gene delivery systems,[22] due to their interesting properties, like large surface area and pore volume, high dispersity, and colloidal durability as well as the easiness of surface functionalization. Ordered mesoporous carbon nanosheets prepared by Jie Wang et al.[23] achieved superb efficiency when applied as electrode for electric double layer capacitors because of their considerable surface area, high conductivity, high graphitization degree, and plentiful mesopores. Sulfonic acid functionalized mesoporous materials[24] have been employed in the advancement of organic synthesis reactions and catalytic protocols, due to their great merits, such as reusability, recoverability, high stability, and ease of co-functionalization with other functional groups to enhance their performance by balancing acidity, basicity, and hydrophobicity.

Another challenging issue of Fe–N–C electrocatalysts is the carbon corrosion, which causes severe problems, such as destroying the active sites in the area of corrosion, loss of porosity, and increasing the charge- and mass-transfer resistance, because of the variations in the electrocatalyst morphology and carbon lattice structure.[25] Enhancing the graphitization degree is a successful way to boost the corrosion resistance of carbon support, and hence increasing the electrocatalyst durability. Furthermore, the high graphitic degree improves the electron transport during the electrocatalysis process of the ORR. Doping with heteroatoms, particularly sulfur (S), has been explored to be an efficient strategy to enhance the ORR catalytic activity of Fe–N–C electrocatalysts,[26,27] due to the remarkable synergistic effect with N dopant, and the potential to facilely replace C atoms when co-doped with N.[28] In addition, the large size and polarizability of S with respect to N cause high degree of spin density, edge strain, and charge delocalization throughout the carbon lattice, resulting in enhancing the conductivity and electron-transfer rate.[29] The doping-induced charge redistribution around the heteroatom dopants alters the O_2 chemisorption mode and debilitates the O–O bonding, hence facilitating the overall ORR process.[30] Besides, the considerably large atomic radius of S creates more defects within the skeleton of the carbon framework, and hence leads to the generation of more active sites for catalyzing the ORR. The defect-induced active sites as a result of the lone pair of electrons in the 3p orbital of S are more adequate for accommodating the lone electron pair of O_2, and thus accelerating the O_2 adsorption.[29]

By Considering all the aforementioned challenges regarding the design and properties of Fe–N–C electrocatalysts (cumbersome procedure, low porosity, insufficient active sites, low graphitization degree, and inconvenient durability), we herein report a pioneered simple, efficient, high-yield, and template/solvent-free synthetic protocol for fabricating Fe–N–C/Fe_3C/C–S–C nanohybrid from low-cost and earth-abundant materials. While the conventional solution-based protocols have some drawbacks, like long-time consumption, low yield, high cost, toxic waste, complexity, and high energy consumption, making the protocol unfavorable for large-scale production and commercial applications, our mechanochemical synthetic approach displays several merits such as avoiding the utilization of solvents and strong acids or bases, high yield, obtaining analytically pure product without the need for further purification, and decreasing the consumption of energy and material; therefore, reducing the production cost. Besides, the yield is obtained in the form of powder, which is ready for the diverse applications without further treatments; and thus overcoming the time-consuming issue and enhancing the sustainability metrics. Therefore, the herein synthetic protocol allows the facile and sustainable synthesis of ORR electrocatalysts on the gram-scale production and enhances the efficiency with respect to the time, material, and energy usage.

In order to construct the Fe–N–C/Fe_3C/C–S–C nanohybrid, ammonium ferric oxalate trihydrate, sucrose, and 2-cyanoguanidine are utilized as iron, carbon, and nitrogen sources, respectively. The influences of incorporating different S-doping levels into the electrocatalyst carbon framework and utilizing various S precursors on the structure, composition, morphology, specific surface area, and ORR activity have been fully elaborated for the first time, aiming to achieve the maximum electrocatalytic activity and durability towards the ORR. Optimizing the synthetic conditions led to the construction of *in situ* formed two-dimensional graphene-like nanosheets with a stable encapsulation of Fe_3C NPs inside the graphitized NS-codoped carbon shells, thus creating an efficient and durable electrocatalyst for the ORR in both acidic and basic environments, since the coated shells safeguard the NPs from leaching out, sintering, or agglomeration. Furthermore, the as-fabricated electrocatalyst displays high specific surface area (SSA), abundant mesopores, high graphitic degree, and significant density of the efficient active sites with uniform distribution throughout the carbon substructure. The synergy of the structural merits described above gives rise to exceptional ORR electrocatalysis (evidenced by the interesting values of E_0, $E_{1/2}$, and diffusion-limiting current density (J_L)), with efficient four electron transfer, high selectivity towards the ORR in the presence of methanol, and excellent durability after 15,000 potential cycles, under both acidic and alkaline working conditions, outperforming the commercial Pt/C (20 wt%) and most of the electrocatalysts reported so far.

View Article Online
DOI: 10.1039/D0TA06987F

2. Results and Discussion

2.1. Materials Characterization

The Fe–N–C/Fe_3C/C–S–C nanohybrid has been fabricated by a mechanochemical solid-state strategy as described in Fig. 1. Four sulfur precursors have been alternatively employed to demonstrate the effect of the S source: two organic sources (thiourea and dibenzyl disulfide (DBDS)), and two inorganic sources ($Na_2S.9H_2O$ and $Na_2S_2O_3.5H_2O$). In order to investigate the effect of S-doping level on the ORR performance of the Fe–N–C/Fe_3C/C–S–C nanohybrid, six samples with multiple contents of S have been synthesized by using different weight percentages of thiourea, aiming to optimize the S-doping level into the electrocatalyst infrastructure to accomplish the ultimate ORR efficiency. The polycondensation between 2-cyanoguanidine and sucrose in the presence of iron source leads to the formation of Fe_3C NPs uniformly dispersed throughout the carbon matrix, and encapsulated in NS-dual doped graphitic shells. This architecture allows indirect-contact ORR electrocatalysis.[31] The constructed graphitic shells encasing the NPs play a fundamental role in preventing their agglomeration during the heat treatment. In addition, they boost the electrocatalytic durability by prohibiting the Fe_3C NPs from leaching under the harsh electrochemical working conditions. High N-doping level (6.47 at%) is achieved which is vital for anchoring more Fe atoms, and hence creating more of the very active Fe–N_x sites. Powder X-ray diffraction (XRD) was performed to identify the crystalline phases present in the as-prepared catalysts. Fig. 2a shows the powder XRD profiles of the electrocatalysts fabricated using multiple S precursors. The electrocatalysts synthesized using organic S sources (thiourea or DBDS) exhibited a broad peak at ≈25.8° indexed to the characteristic (002) planes of graphitic carbon,[32] demonstrating the formation of amorphous carbon architectures in these two catalysts. On using an inorganic source (Na_2S or $Na_2S_2O_3$), the carbon peak slightly shifted to a higher 2θ value (≈26.45°), and the peak intensity became sharper and narrower, indicating the high graphitization degree of the carbon structures in these materials. This indicates that employing an inorganic S precursor during the electrocatalyst preparation could induce a higher degree of carbon graphitization. The remaining diffraction peaks are ascribed to Fe_3C phase (PDF #96-901-2188). Fig. S1† compares of the XRD profile of the Fe–N–C/Fe_3C/C–S–C nanohybrid with the reference phase.

The crystallites size is an important parameter for characterizing a powdered material. we used Scherrer equation to estimate the crystallites size from the peak of the highest intensity.

$$D = (K\lambda) / (\beta \cos \theta)$$

Where D is the crystallite size in nm, K is a shape constant (0.9), λ is the wavelength of the X-ray source (λ= 0.15406 nm in the case of Cu (Kα) radiation), β is the full width at half-maximum (FWHM) of the diffraction peak in radians, and θ is the peak position in radians. The calculated average crystallites size of the prepared catalysts in the case of using organic S sources (thiourea and DBDS) was 9.47 and 11.63 nm, respectively, meanwhile it was 21.23 and 22.89 nm when inorganic S sources ($Na_2S.9H_2O$ and $Na_2S_2O_3.5H_2O$) were utilized to prepare the catalyst. It very clear that the use of organic S sources for doping S into the electrocatalyst infrastructure led to the excellent dispersion of the nanoparticles (NPs) throughout the carbon matrix, as indicated from the smaller sizes of the NPs (9.47 and 11.63 nm). Since these NPs are Fe_3C, which are very active for catalyzing the ORR, the high dispersion and smaller size of these NPs are partially responsible for the high electrocatalytic activity of the materials synthesized from organic S sources as will be discussed in the electrochemical evaluation section, where the high dispersion and smaller NPs size create more active sites for catalyzing the ORR. The data obtained from analyzing the XRD patterns emphasize that selecting the appropriate S source is a fundamental parameter for boosting the catalytic performance of a material for the ORR, where it has a great influence on controlling the NPs size and their dispersion within the carbon skeleton.

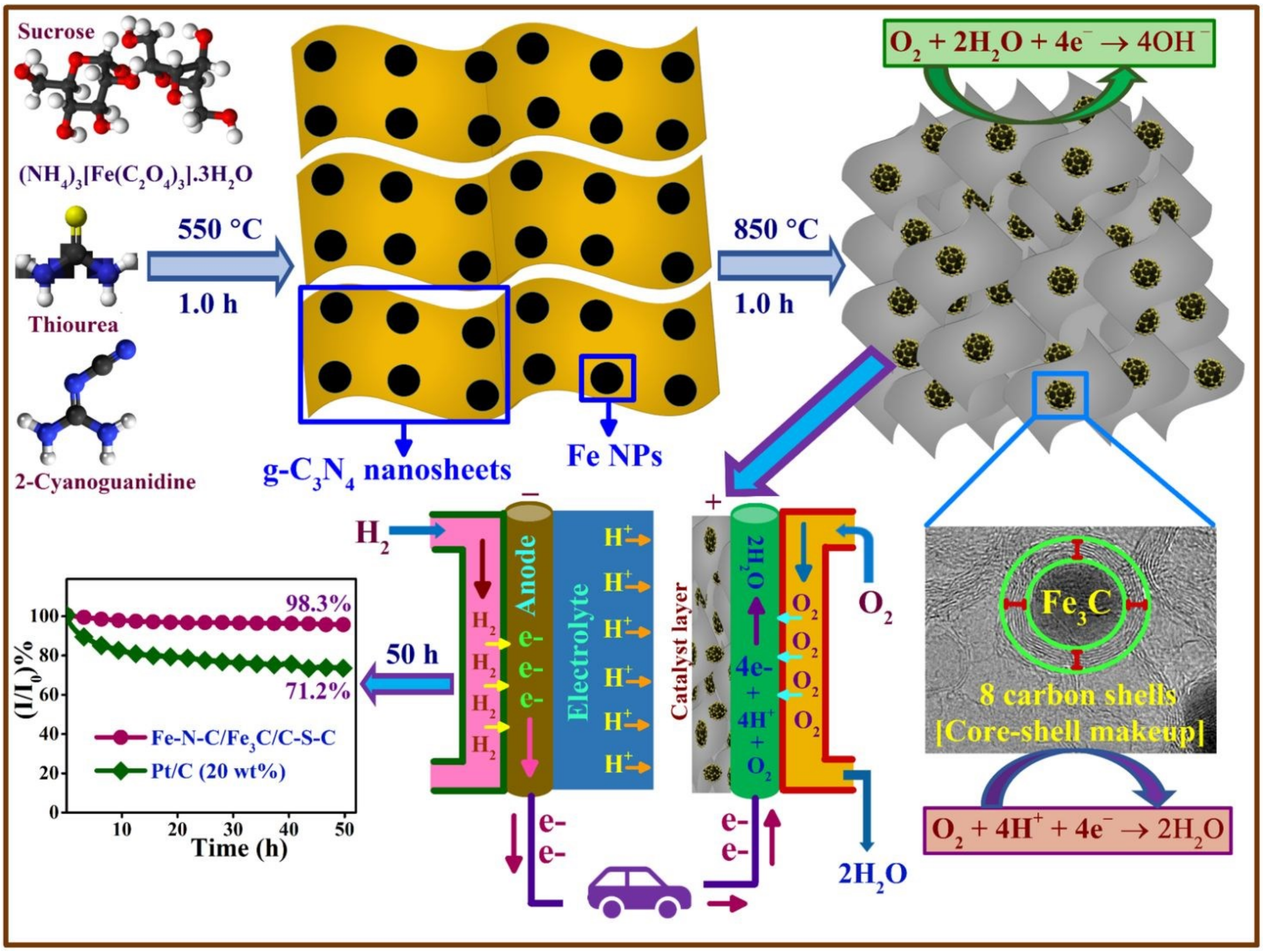

Fig. 1 Schematic diagram for the synthetic procedure of Fe–N–C/Fe_3C/C–S–C nanohybrid.

Fig. 2b displays the powder XRD patterns of the electrocatalysts synthesized using various weight proportions of thiourea. The peak at ≈26° corresponds to the (002) facets of carbon. The remaining peaks in the electrocatalysts fabricated without S-doping and in the presence of 16 and 40

View Article Online
DOI: 10.1039/D0TA06987F

wt% of thiourea are assigned to the orthorhombic Fe_3C (PDF #96-901-2188) phase, except the small peaks at 2*θ* of 29.9° and 33.7° in the 40 wt% sample, which are ascribed to the hexagonal FeS (PDF #96-100-9044) phase. The low intensity of the peaks related to FeS indicates the small content of FeS in this sample. It is noteworthy that the intensities of the peaks correlated to the Fe_3C phase at 2*θ* of 37.7°, 49.1°, and 51.8° diminished when the thiourea ratio was raised from 16 to 40 wt%; meanwhile, the peaks at 54.4° and 58° disappeared, indicating the lower content of Fe_3C phase. More importantly, when the proportion of the thiourea was increased to 80 wt%, all of the peaks mentioned above completely disappeared; and instead, new diffractions peaks were formed at 2*θ* of 29.9°, 33.7°, and 53.1° (indicated by the blue rectangles in Fig. 2b), which correspond to the hexagonal FeS (PDF #96-100-9044).

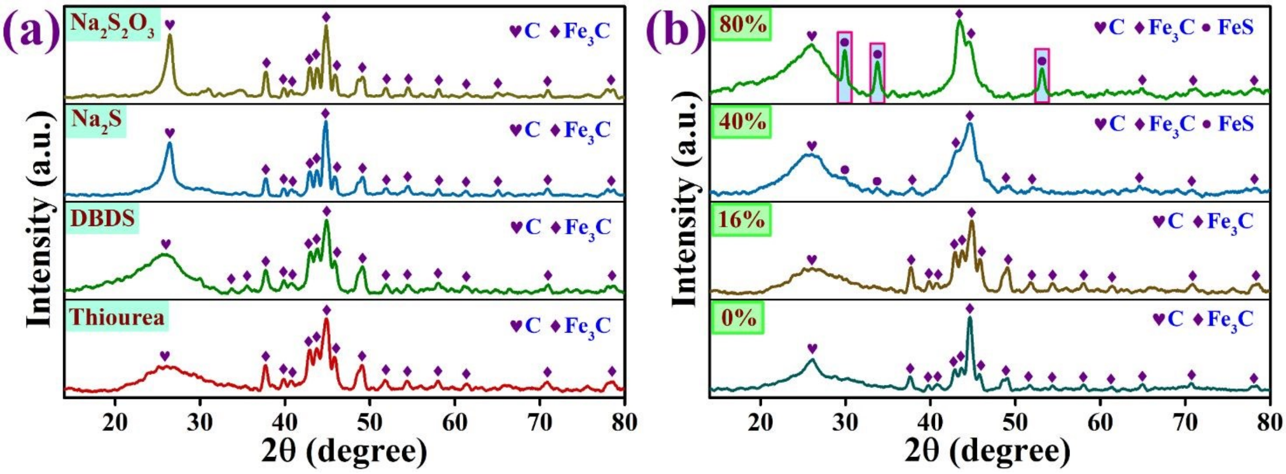

Fig. 2 Powder XRD profiles of Fe–N–C/Fe_3C/C–S–C nanohybrids fabricated utilizing various S precursors (a), and different weight proportions of thiourea (b). The peaks highlighted by the blue rectangles in Fig. 2b represent the peaks related to the hexagonal FeS phase.

Fig. 3a and 3b display the Raman scattering spectra of the different innovated electrocatalysts. It is apparent that all catalysts exhibit two predominant and distinctive scattering peaks at 1340 and 1578 cm^{-1}, which are related to the existence of disordered sp^3-hybridized carbon (D band) and graphitic sp^2-bonded carbon atoms (G band) in the graphitic network, consecutively.[33] The intensity ratio between the two bands (I_G/I_D) provides a sensitive metric to assess the crystallinity degree and lattice distortion of the carbonaceous nanomaterials. It is noticeable from Fig. 3a that the electrocatalysts synthesized using organic S precursors offered much lower I_G/I_D ratios (0.998 and 1.018) than those fabricated using inorganic sources (1.409 and 1.444). This suggests that utilizing an inorganic S precursor enhances the graphitization degree of the obtained catalyst, which agrees with the conclusions realized from the XRD analysis (Fig. 2a). In contrast, the use of organic S precursors induces the formation of defects and disorderliness within the electrocatalyst

View Article Online
DOI: 10.1039/D0TA06987F

nanostructure, revealing the presence of abundant graphene edges/defects and pores in the Fe–N–C/Fe_3C/C–S–C nanohybrid prepared from organic S sources. The defects arise from incorporating the heteroatoms into the carbon framework. Since the defects serve as catalytic active sites, because they can modify the nature of bonding and adjust the electronic as well as surface properties of the electrocatalyst,[34] the electrocatalyst with more defects is expected to display improved ORR activity, compared to that of less defects. The electrocatalyst synthesized using thiourea showed an I_G/I_D ratio almost equal to unity (0.998), suggesting that its substructure has equal degrees of disorderliness and graphitization. The graphitization enhances the electric conductivity, while the imperfections in the carbon lattice provide active centers for the ORR. The two small peaks discerned at ≈2677 and ≈2886 cm^{-1} can be assigned to the 2D and D + G bands.[35] The 2D band emanates from a two-phonon and second-order scattering process,[36] meanwhile the combination D + G is attributed to the defect-induced double resonance scattering process.[37] The intrinsic properties of the as-prepared electrocatalysts from monolayer to multilayer graphene can be identified from the spectral profile of the 2D band.[38] The low intensity and broadness of the 2D band in the case of using thiourea or DBDS signify the construction of a thick graphitic matrix with multilayers. In contrast, the presence of Na_2S or $Na_2S_2O_3$ led to the formation of a thin-layer nanostructure, as evidenced by the sharp 2D band (Fig. 3a). It can be concluded that the use of the proper S precursor contributes to the degree of graphitization and number of defects, as well as the thickness of the *in situ* constructed graphene network, which significantly influence the ORR activity and stability. On the other hand, increasing the proportion of thiourea from 0 to 80 wt% resulted in a gradual increase of the I_G/I_D ratio from 0.991 to 1.048, revealing that increasing the S-doping level led to a slight enhancement in the electrocatalyst graphitization degree (Fig. 3b). The 2D and D + G bands are approximately the same for all catalysts. In addition, another peak was observed at ≈2425 cm^{-1}, associated with the D + D" band; which is the combination of a phonon ascribed to the section accountable for the D peak and a second phonon attributed to the branch in charge of the D" peak.[39] D" correlates with a phonon related to the in-plane longitudinal acoustic branch near the K point.[40]

View Article Online
DOI: 10.1039/D0TA06987F

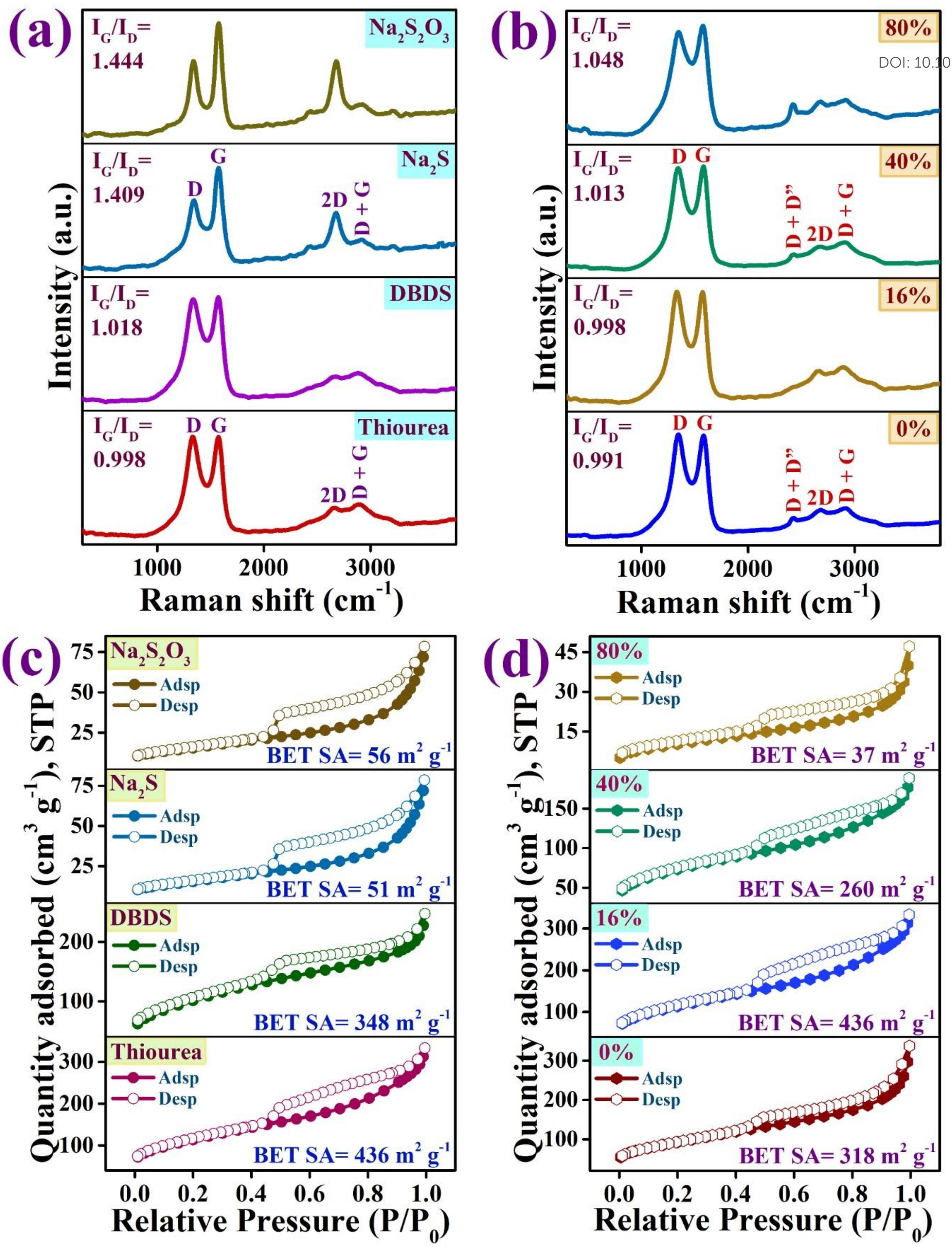

Fig. 3 (a and b) Raman spectra of Fe–N–C/Fe_3C/C–S–C nanohybrids synthesized utilizing various S precursors (a), and different weight proportions of thiourea (b). (c and d) N_2 adsorption/desorption isotherms of Fe–N–C/Fe_3C/C–S–C nanohybrids prepared utilizing various S precursors (c), and different weight ratios of thiourea (d).

Fig. 3c and 3d show the nitrogen adsorption/desorption isotherms of the various fabricated materials. The SSAs were estimated by using the Brunauer-Emmett-Teller (BET) calculations. The samples synthesized using different S sources offered type-IV isotherms with insignificant uptake at small relative pressures ($P/P_0<0.1$) and well-defined hysteresis loops at higher P/P_0 ratios ranging from 0.45 to 1.0, suggesting that mesopores predominantly exist. The electrocatalysts synthesized utilizing thiourea, DBDS, Na_2S, and $Na_2S_2O_3$ displayed different SSAs of (436, 348, 51, and 56) $m^2\ g^{-1}$, respectively, implying that selecting the proper S precursor for S-doping into the electrocatalyst substructure is essential for maximizing its SSA, and hence promoting its efficiency for ORR. Investigating the pore size distribution (PSD) showed that the synthesized materials have hierarchical pore structure, where the electrocatalyst synthesized using thiourea contained the maximum quantity of mesopores with diameters centered at 3.9 nm (Fig. S2†) and the largest total pore volume of 0.452 $cm^3\ g^{-1}$ (Table S2†). Such plentiful numbers of mesopores indicate the presence of many structural deficiencies within the carbon substructure of the Fe–N–C/Fe_3C/C–S–C nanohybrid, which agrees well with the Raman results. In addition, the electrocatalysts prepared utilizing organic S precursors (thiourea and DBDS) displayed the largest micropore surface areas (35 and 37 $m^2\ g^{-1}$) and micropore volumes (0.023 and 0.024 $cm^3\ g^{-1}$), respectively (Table S2†). Since the portion of micropores commonly describes the density of hosted active sites, where the ORR active sites predominantly exist in micropores,[41] the electrocatalysts constructed utilizing thiourea and DBDS are anticipated to hold higher numbers of active sites, and hence much enhanced ORR performance.

Interestingly, not only the S precursor has a major effect on the SSA, but also the proportion of doped-S as shown in Fig. 3d. The S-free electrocatalyst exhibited SSA of 318 $m^2\ g^{-1}$. When S was introduced into the electrocatalyst framework at a certain proportion, the SSA was significantly enhanced to 436 $m^2\ g^{-1}$. However, increasing the S-doing level over a specific ratio had a detrimental influence on the SSA, where the SSAs were reduced to 260 and 37 $m^2\ g^{-1}$ when 40 and 80 wt% of thiourea, respectively, were employed during the solid-state synthetic process. Fig. S3† shows the PSD for the electrocatalysts established using different weight proportions of thiourea, where the electrocatalyst synthesized at 16 wt% manifested the maximum number of mesopores. It obvious that increasing the proportion of thiourea from 16 to 80 wt% resulted in a detrimental influence on the electrocatalyst mesoporosity, where the electrocatalyst prepared at 80 wt% had very low total pore volume (0.054 $cm^3\ g^{-1}$) (Table S2†). It can be concluded that employing the appropriate S precursor and doping the suitable quantity of S into the electrocatalyst framework are of utmost importance for maximizing the BET SSA and mesoporosity, and hence maximizing the electrocatalyst performance for the ORR. Such ideal porous substructure with large SSA, well-balanced micro-/mesoporosity, and high graphitization level could partially explain the high ORR performance of Fe–N–C/Fe_3C/C–S–C nanohybrid, where: 1) the large SSA can host tremendous numbers of active centers; 2) the interconnected 2D mesoporous framework ensures the accessibility of the reactants to the active sites, and therefore guarantees the efficient mass transfer; 3) the good graphitization level of the carbon substructure accelerates the electron transport and promotes the corrosion resistance of the carbon matrix, thus conserving the active sites from dissolution.

Because the catalytic performance of a material is greatly influenced by its morphology, we first monitored the morphological evolution of the various electrocatalysts by field-emission scanning electron microscopy (FESEM) imaging (Fig. 4a–g), and correlated the obtained morphologies with the ORR performance. The electrocatalyst prepared in the presence of $Na_2S_2O_3$ displayed one-dimensional nanorods-like morphology (the nanorods are indicated by green arrows). In the case of Na_2S, the material exhibited irregular morphology, accompanied by the presence of nanorods in some locations of its surface (green arrows in Fig. 4b). In addition, the low magnification images (Fig. S4a† and S4b†) offered disordered carbon structure with severe agglomeration on the materials surface, when inorganic S precursors were utilized. The catalyst prepared in the presence of DBDS (Fig. 4c and S4c†) showed nanosheets-like morphology, where the carbon layers were densely stacked, resulting in decreasing the porosity, and hence the inability to expose all the active sites to the electrolyte and inhibiting the mass transport during the ORR. On the other hand, the fabricated nanomaterial from thiourea (Fig. 4d and S4d†) presented 3D hierarchical graphene-like architecture with ultrathin carbon nanosheets protruding from electrocatalyst surface, leaving highly porous tunnels in between. Such *in situ* formed 3D nanostructure with open spaces greatly boosts the ORR catalytic activity and durability, since it possesses enormously greater interfacial contact area with the support than nanotubes, nanowires, or NPs. The high contact area promotes the electron transfer between the electrocatalyst surface and reactants, and reinforces the adhesion between the electrocatalyst and the support. In addition, the high porosity accelerates the mass transfer during the ORR electrocatalysis. Further, this electrocatalyst displayed homogeneous dispersion of the NPs throughout the carbon substructure (Fig. S5†). It can be deduced that thiourea is the optimum precursor for incorporating S into the electrocatalyst framework, where it prefers the construction of a hierarchically porous infrastructure with high BET SSA. Conversely, employing the other precursors led to the formation of malformed morphologies with less porosities and lower BET SSAs.

The differences in the properties of the obtained catalysts, such as morphology, graphitization degree and SSA, as a result of changing the S source can be interpreted as follows: In our synthetic approach, we used a temperature–programmed reaction to induce the reaction between the precursors, where the precursor mixture was firstly heated under flowing argon gas as an inert atmosphere at 550

DOI: 10.1039/D0TA06987F

°C for 1 h, at heating rate of 2 °C min^{-1} then pyrolysed at 850 °C for 1 h, at heating rate of 5 °C min^{-1}. The differences in the nature and properties of organic and organic S sources, such as melting point and decomposition behavior caused great differences in the properties of the products, such as specific surface area, morphology, and graphitization degree. For the example, in the case of thiourea (melting point is 182 °C) as an organic S source, with increasing the temperature, thiourea begins to decompose with the evolution of NH_3 and H_2S, and converts into g–C_3N_4 at 550 °C. [42] The evolved gases play a significant role in enhancing the porosity of the final product and increasing its surface area. Increasing the calcination temperature over 550 °C led to the complete decomposition of g–C_3N_4. Dibenzyl disulfide decomposes into H_2S and other sulfur-containing compounds above 250 °C.[43] In the case of sodium thiosulfate pentahydrate ($Na_2S_2O_3.5H_2O$, melting point is 48.3 °C) as an example of an inorganic S source: the first water molecule detaches at 44.1 °C. At temperature of 131.8 °C, the rest water molecules detach sequentially. On further heating above 302.4 °C, the anhydrous material begins to decompose.[44] Sodium sulfide nonahydrate ($Na_2S.9H_2O$) begins to lose its water molecules down to monohydrate with increasing the temperature until 200 °C. The resulted $Na_2S.H_2O$ begins to decompose at 700 °C.[45] Since all reaction conditions are the same except that the S precursor is different, the dissimilarities in the properties of the various products are attributed to the differences in the nature and thermal decomposition behavior of the organic and inorganic S sources as have been demonstrated above. In addition, the herein utilized inorganic S sources have sodium metal in their structure, meanwhile the organic ones do not have. The presence of sodium resulted in much enhancement in the graphitization degree[46] of the catalysts prepared from inorganic sources comparing to those prepared from organic ones as have been shown from the XRD and Raman data (Fig. 2a and 3a). For that reason, the catalysts prepared from inorganic sources exhibited higher degree of graphitization comparing to those prepared from organic ones. Based on the results obtained here, the graphitization degree can be controlled by the careful selection of the S precursor. In the applications where both of disorderliness and graphitization are required to exist in the material such as in the ORR application, the organic S sources will be the suitable candidate, meanwhile in those applications where the material should have very high degree of graphitization, the inorganic source will be the proper candidate for that purpose. The products obtained from the use of organic S sources had high surface area and more porosity because the decomposition of organic sources is usually accompanied by the evolution of many gases, which resulted in enhancing the surface area and porosity of the obtained materials, comparing to those prepared from inorganic sources.

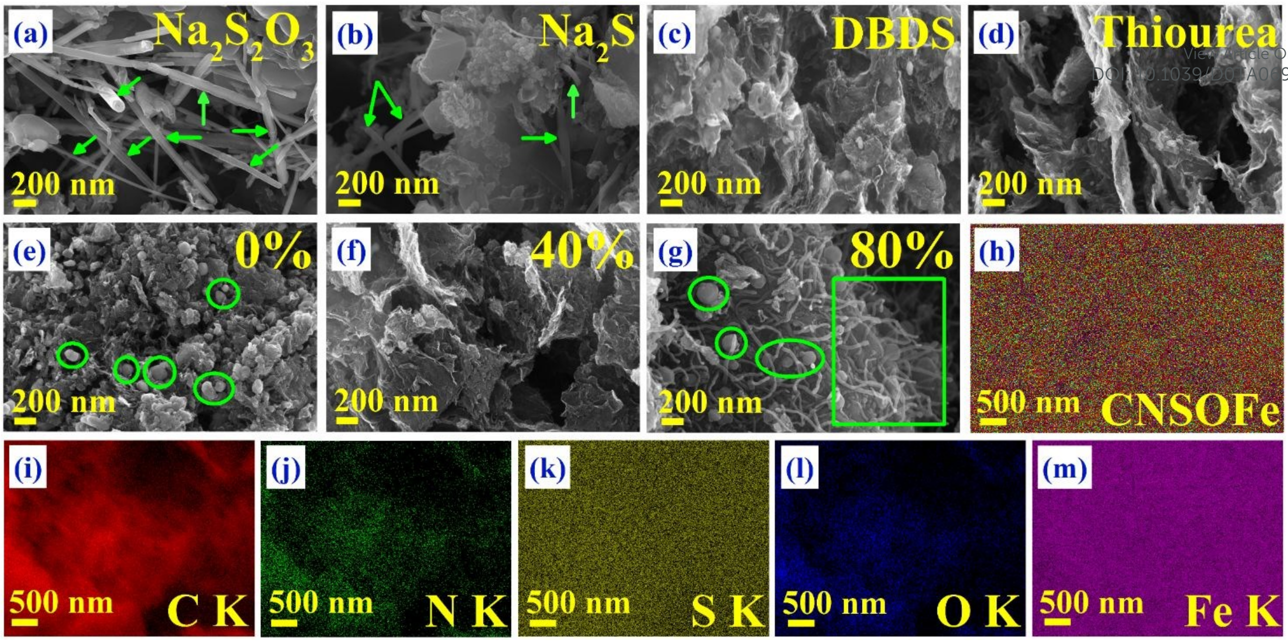

Fig. 4 (a–d) FESEM images of Fe–N–C/Fe_3C/C–S–C nanohybrids fabricated using different S precursors. The green arrows in Fig. 3a and b indicate to the nanorods grown on the electrocatalyst surface. (e–g) FESEM images of Fe–N–C/Fe_3C/C–S–C nanohybrids synthesized utilizing various weight proportions of thiourea. The green circles in Fig. 3e and g show the NPs agglomeration, whereas the green rectangle in Fig. 3g exhibits the CNTs grown on the electrocatalyst surface. (h) Total elements mapping image of Fe–N–C/Fe_3C/C–S–C nanohybrid. (i–m) Energy dispersive X–ray spectroscopy elemental mapping images of C, N, S, O, and Fe elements in the Fe–N–C/Fe_3C/C–S–C nanohybrid.

Fig. 4e–g shows the effect of using different proportions of thiourea on the materials morphology. The sample prepared without S-doping showed distorted morphology with serious agglomeration of NPs (indicated by the green circles in Figs. 4e and S7a†) which resulted in lowering the contact surface area with the electrolyte, inhomogeneous distribution of the NPs, and lessening of the number of active sites, and therefore inferior ORR activity. When S was incorporated into the electrocatalyst infrastructure in small proportions, there was much enhancement in the morphology as can be clearly seen in Figs. 4d and S6b†. In addition, the NPs were uniformly distributed throughout the carbon matrix (Fig. S5†). Consequently, the inclusion of S into the electrocatalyst carbon framework is essential for the homogenous distribution of NPs and obtaining uniform nanosheets morphology with large BET SSA and high porosity. The electrocatalyst fabricated with 40 wt% of thiourea (Figs. 4f and S6c†) exhibited similar morphology to that of 16 wt%; however, the nanosheets were relatively stacked together, which resulted in lowering the porosity and SSA of the electrocatalyst, and hence weakening its catalytic activity for the ORR. Using very high proportions of thiourea, such as 80 wt%, caused plenty of carbon nanotubes (CNTs) to grow on the material surface as indicated by the green rectangle in Fig. 4g. Furthermore, significant agglomeration of the NPs occurred (highlighted by the green circles). The generation of CNTs and agglomeration of NPs resulted in much contraction in the BET SSA of the catalyst (37 m^2 g^{-1}, Fig. 4d), and hence poor ORR activity. The FESEM images at low magnifications for the samples synthesized without S-doping and with high weight ratio of thiourea (80 wt%) (Fig. S7†) showed severe agglomeration of the NPs, which led to diminishment in the number of active sites and BET SSA. The variations in morphology resulted from incorporating different S contents into the electrocatalyst carbon matrix will undoubtedly influence on the ORR catalytic activity, as will be explained in the electrochemical evaluation section. The elemental energy-dispersive spectroscopy images (Fig. 4h–m) of the optimal electrocatalyst demonstrate that the C, N, S, O, and Fe elements were homogenously distributed throughout the electrocatalyst substructure and no agglomeration of NPs was observed.

The transmission electron microscopy (TEM) and high-resolution TEM (HRTEM) images of Fe–N–C/Fe_3C/C–S–C nanohybrid (Fig. 5) show that the electrocatalyst has nanosheets-like morphology and consists of several NPs embedded in the carbon framework. The HRTEM image (Fig. 5b) reveals the establishment of a perfect core-shell infrastructure within the electrocatalyst carbon network, where the Fe_3C NPs are enveloped by 8 layers of graphitic shells. Since the NPs tend to agglomerate/sinter during either the annealing at high temperature or electrocatalytic work for long periods, the existence of these carbon shells could act as a successful safeguarding layer to prevent the NPs from agglomeration, and to boost the electrocatalyst durability. Moreover, the graphitic shells display conspicuous stripes, indicating their high crystallinity, which is beneficial for promoting the electron conductivity and increasing the corrosion resistance. Fig. 5b distinctly shows that the graphitic carbon layers are interconnected and spread in all directions around the encapsulated NPs. This architecture plays a fundamental role in supplying free space and compendious diffusion paths for the reactants and intermediates during the ORR electrocatalysis, which ultimately promotes both charge transport and mass transfer, hence maximizing the ORR efficiency. The HRTEM at another position (Fig. 5c) corroborates the multidirectional nature of the graphitic domains. The clear lattice fringes of the graphitic domains (Fig. 5b, c, and f) assure the high graphitization degree of the carbon matrix, which is vital for facilitating the electron transfer and improving the corrosion resistance.

The HRTEM image presented in Fig. 5d divulges that the formed graphitic substructure is porous and imperfect, suggesting the existence of structural defects within the Fe–N–C/Fe_3C/C–S–C substructure. The inset is the fast Fourier transform (FFT) pattern. These defects perform a vital role in enhancing the efficiency of the ORR, where they alter the distribution of the electron density and electronic charge of the electrocatalyst,[34] which facilitates the oxygen adsorption and enervates the O–O bonding. More importantly, the defects are primarily induced by the heteroatom doping into the carbon nanomaterials; and hence they become active centers for the ORR. Fig. 5e clearly shows that

View Article Online
DOI: 10.1039/D0TA06987F

the graphitic shells encapsulating the Fe_3C NPs are porous and contain many defects, which is because of the N and S doping into those shells. This confirms that the heteroatoms (N and S) were doped into the carbon shells. The porous nature of the graphitic shells is believed to promote the mass transfer to the Fe_3C cores during the electrocatalysis process. The area highlighted by the purple rectangle in Fig. 5f reveals that the electrocatalyst has porous carbon infrastructure, which effectively promotes the loose transfer of oxygen molecules within the electrocatalyst layers, hence catalyzing the electrode reactions. Furthermore, the porous nanostructure provides the electrocatalyst with intriguing characteristics that are tremendously beneficial for upgrading the electrocatalyst performance for the ORR, such as the proficient exposure of the active sites, increasing the surface permeability, and enhancing the mass transport during the ORR process.[21] These properties result in a full exploitation of the electrocatalyst.

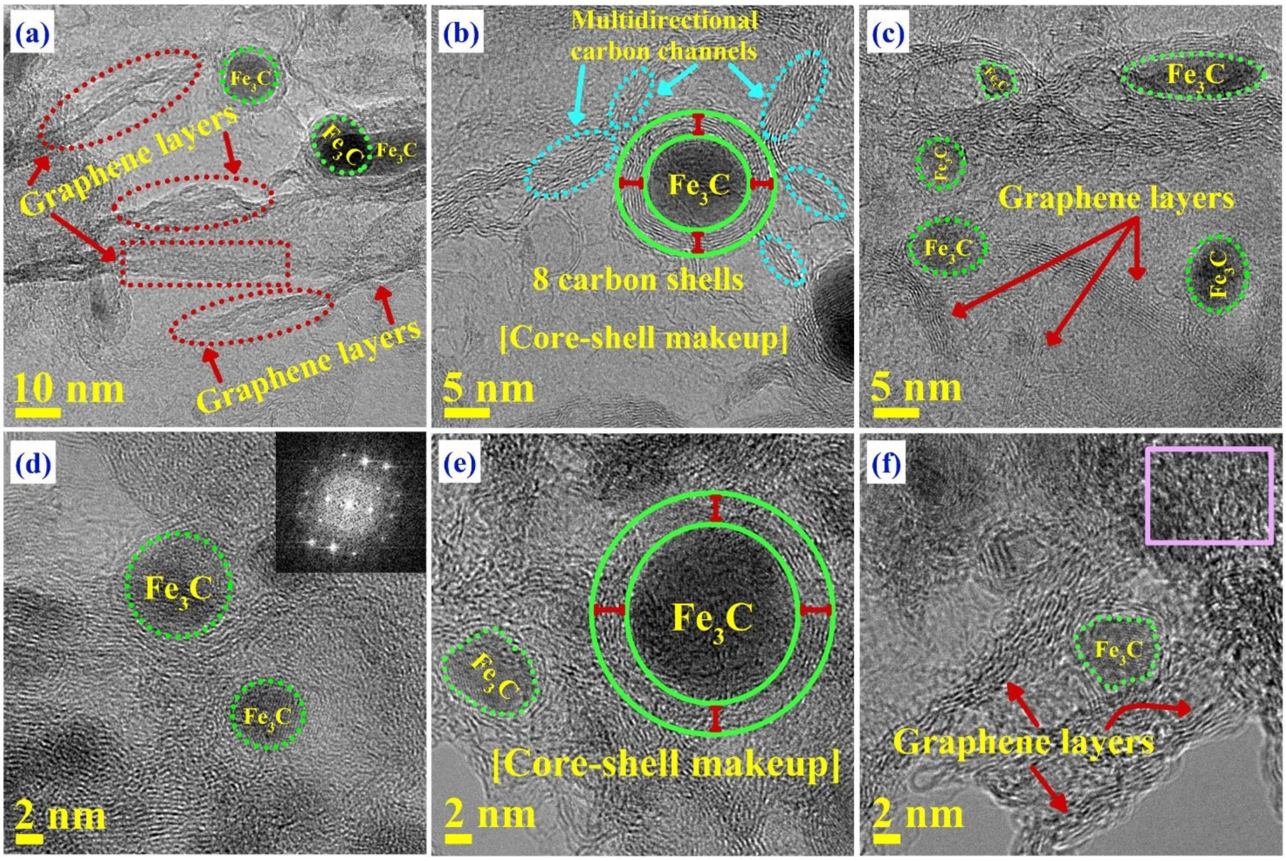

Fig. 5 (a) TEM image and (b–f) HRTEM images of Fe–N–C/Fe_3C/C–S–C nanohybrid at different locations. The inset in Fig. 4d is the fast Fourier transform (FFT) pattern.

The HRTEM image at another location (Fig. 6a) further confirms the core-shell structure, and demonstrates the multidirectional nature of the carbon channels. In addition, we recorded the lattice image (Fig.6b) by the inverse fast Fourier transform (IFFT) for the highlighted area by the yellow rectangle in Fig. 6a, in order to ascertain the d-spacing values between the carbon layers. Fig. 6c

View Article Online
DOI: 10.1039/D0TA06987F

manifests the corresponding line scan profile for the selected area in the IFFT image of the electrocatalyst. To accurately delineate the d-spacing, the distance between 4 carbon layers was calculated to be 1.42 nm; therefore, the average distance between two layers is 0.335 nm. This lattice fringes can be assigned to the (002) interplanar d-spacing of graphite (PDF #96-901-2231), which corroborates that the electrocatalyst had a graphitic carbon structure. This further substantiates the construction of multilayer-graphene in accordance with the outcomes from the XRD and Raman characterizations. To authenticate the composition of the NPs incorporated into the electrocatalyst substructure, the HRTEM image (Fig. 6d) was accomplished at a single NP encapsulated in the graphitic shells, and the corresponding IFFT image is depicted in Fig. 6e. The IFFT image discloses that the lattice fringes of the encapsulated NPs are highly perspicuous, suggesting that they have crystalline nature. The line scan analysis (Fig. 6f) of the highlighted area in the IFFT image of the encased NP reveals that the lattice spacing between the indicated pink lines is 1.21 nm. This value corresponds to the interplanar distance between 6.0 planes. Accordingly, the average lattice spacing is 0.201 nm; which can be earmarked for the interspacing of (031) lattice fringes of Fe_3C (PDF #96-901-2188). From the outcomes of the HRTEM and IFFT images, it can be concluded that the incorporated NPs within the carbon matrix of the fabricated electrocatalyst are the orthorhombic Fe_3C.

The high-angle annular dark field scanning TEM (HAADF-STEM) image (Fig. 6g) and the corresponding energy dispersive X-ray (EDX) elemental mapping images (Fig. 6h–l) distinctly show that the C, N, S, O, and Fe elements were uniformly dispersed throughout the electrocatalyst carbon infrastructure. The intense and bright zones in the HAADF-STEM image represent the Fe atoms, because Fe atoms have much higher electron density than those of the remaining elements (C, N, S, and O).[47] It is obvious that the C and Fe atoms predominantly exist together in the NPs locations, which further confirms that these NPs are Fe_3C. In addition, the N and S atoms are present in the positions surrounding the NPs in the elemental mapping images, providing evidence that N and S were successfully doped into the graphitic shells that encapsulate the NPs, as well as into the whole electrocatalyst carbon framework. The electrocatalyst synthesized utilizing $Na_2S_2O_3$ showed excessive agglomeration of the NPs (Fig. S8†) which is highly deleterious for ORR performance. Similarly, the electrocatalyst obtained without S-doping displayed severe agglomeration of the NPs (Fig. S9†), in agreement with the FESEM observations. Based on the different characterization results discussed above, it can be concluded that incorporating S into Fe–N–C electrocatalyst considerably modified the morphology, porosity, surface area, and surface atomic composition of the obtained electrocatalyst, which significantly affected the ORR performance.

View Article Online
DOI: 10.1039/D0TA06987F

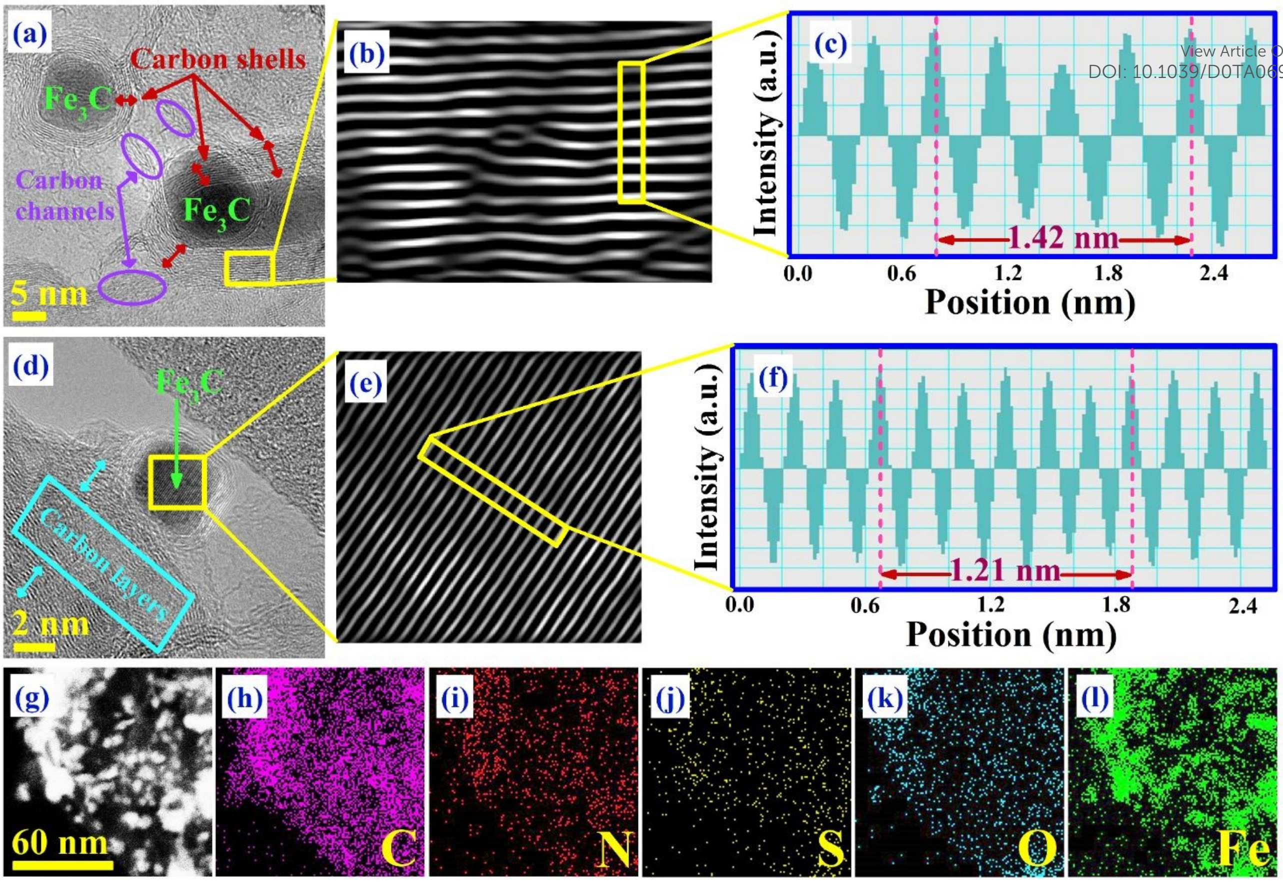

Fig. 6 (a and d) HRTEM images of Fe–N–C/Fe_3C/C–S–C nanohybrid at different positions. (b) The lattice image recorded by the inverse fast Fourier transform (IFFT) for the highlighted area by the yellow rectangle in Fig. 5a. (c) Corresponding line scan profile for the selected area in Fig. 5b. (e) The IFFT image of the NP indicated by the yellow rectangle in Fig. 5d. (f) Line scan analysis of the highlighted area in Fig. 5e. (g) HAADF-STEM image, and (h–l) corresponding energy dispersive X-ray elemental mapping images of the Fe–N–C/Fe_3C/C–S–C nanohybrid.

The different oxidations states and bonding configurations of N, S, and Fe were identified by means of the X-ray photoelectron spectroscopy (XPS) analysis. Fig. 7a displays the XPS survey spectra of the electrocatalysts synthesized using thiourea, DBDS, and $Na_2S_2O_3$. Table S3† shows the atomic proportions of C, N, S, O, and Fe in the examined samples. The sample prepared with thiourea possessed the highest surface atomic percentage of N (6.47 at%), whereas that prepared with $Na_2S_2O_3$ had the lowest content (2.31 at%). The remarkable N content in the optimal electrocatalyst is extremely beneficial for the ORR, because it creates greater numbers of active sites, and hence increasing the density of active sites. In addition, the high N content facilitates anchoring of more Fe atoms, which leads to creating more of the highly active Fe–N_x centers.[48] The deconvolution of the N 1s spectrum revealed the presence of five bonding configurations of N located at binding energies of 398.3, 399.2, 400.3, 401.3, and 403.2 eV, which correlate with the pyridinic–N, Fe–coordinated N (N_x–Fe), pyrrolic–N, graphitic–N, and oxidized–N, consecutively.[49] (Fig. 7b). Since the content of each kind of N species plays a crucial role in determining the electrocatalyst performance towards the ORR, the proportions of the different nitrogen bonding configurations were calculated, and inserted in Table S4†. Interestingly, the electrocatalyst obtained from thiourea not only possessed the highest proportion of N (6.47 at%), but also had the maximum contents of pyridinic–N (1.85 at%) and N_x–Fe (1.49 at%), among all the fabricated electrocatalysts. Pyridinic–N has been approved as an active center for the ORR.[3] The remarkable amelioration of the pyridinic–N implies that our nanohybrid possesses abundant exposed edge regions, which can be doped with N, resulting in the creation of numerous edge-nitrogen, e.g., pyridinic–N.[48] This architecture is greatly advantageous for the ORR catalysis, because the edge sites are much more easily accessed by the reactants and electrolyte than the bulk sites. The N_x–Fe species are essential active sites for the ORR in acidic and alkaline environments.[50] Furthermore, the catalyst produced from thiourea showed the highest content of graphitic–N (1.07 at%), indicating that the graphitic carbon includes high level of N doping. The graphitic–N serves as an efficient active center for the ORR through a direct four-electron transfer route, where the cleavage of the O–O bond tends to occur easily, due to the small energy barrier of the graphitic–N for O_2 adsorption.[51] Moreover, both of the pyridinic–N and graphitic–N can regulate the chemical/electronic nature of the neighboring carbon atoms, and hence improving the ORR activity.[52] The XPS survey spectra and the deconvolution of N 1s spectrum for the electrocatalysts prepared using 16 and 40 wt% of thiourea are displayed in Figs. S10† and S11†. The increase in the proportion of thiourea resulted in reducing the N-doping level from 6.47 to 4.17 at%.

The deconvoluted S 2p spectrum divulged four distinct peaks corresponding to the various S species present in the electrocatalysts (Fig. 7c). The peak located at binding energy of 162.1 eV (highlighted by light purple color in Fig. 7c) is ascribed to the S^{2-} moieties bonded with Fe atoms (FeS_x). The presence of FeS_x coordination greatly promotes the ORR performance, since Fe–S sites have been shown to be proficient active centers for the ORR in both acidic and basic electrolytes.[53] The peaks situated at 163.6 and 164.9 eV are ascribed to the S $2p_{3/2}$ and S $2p_{1/2}$ orbitals in the C–S–C configuration. The thiophene (C–S–C) species have been reported as efficient active sites for enhancing the ORR electrocatalysis.[27,41] The peak at the highest binding energy (168.6 eV) is associated with the oxidized S groups (C–SO_x–C), which have been revealed to promote the adsorption of O_2 molecules,[54] and thus contribute to enhancing the ORR process. Table S5† displays the proportions of the various S configurations in synthesized electrocatalysts. The above XPS results distinctly show that N and S atoms were successfully incorporated into the electrocatalyst carbon infrastructure. Fig. S12† displays the deconvolution of S 2p spectrum for the electrocatalysts prepared using 16 and 40 wt% of thiourea. As expected, the increase in the proportion of thiourea resulted in promoting the S-doping level from 0.97 to 1.90 at% (Table S3†).

View Article Online
DOI: 10.1039/D0TA06987F

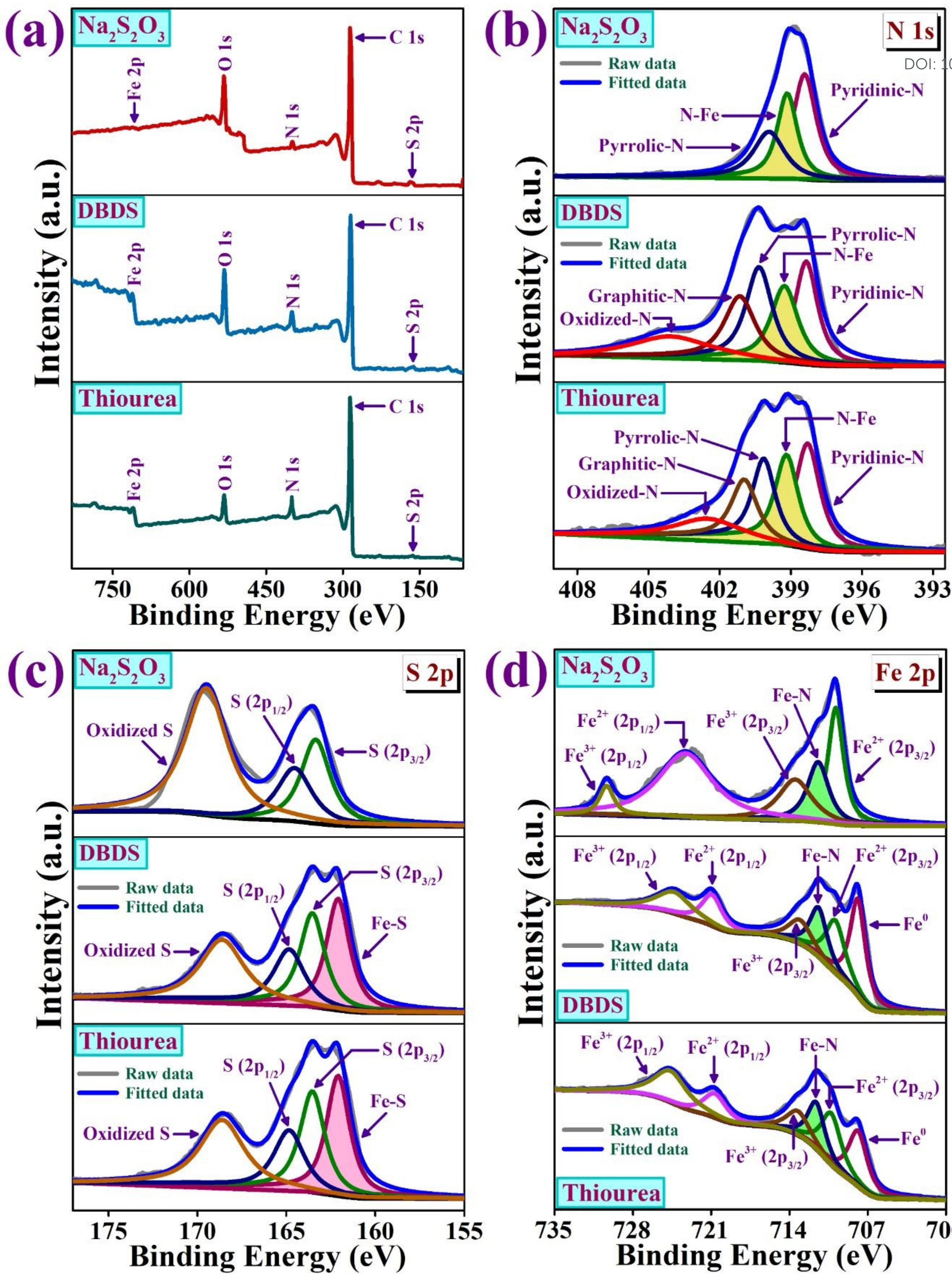

Fig. 7 (a) XPS survey spectrum of Fe–N–C/Fe_3C/C–S–C nanohybrids fabricated utilizing different S precursors. (b–d) fitted high-resolution XPS spectra of the N 1s (b), S 2p (c), and Fe 2p (d); in Fe–N–C/Fe_3C/C–S–C nanohybrids synthesized using various S precursors.

The high-resolution Fe 2p spectrum showed six deconvoluted peaks (Fig. 7d). The peak detected at the lowest binding energy (708 eV) is imputed to the zero-valence Fe. The peaks at 710.1 and 713.4 eV are assigned to the $2p_{3/2}$ orbitals of Fe^{2+} and Fe^{3+} moieties, whereas those observed at

720.7 and 724.9 eV are attributed to the $2p_{1/2}$ orbitals of Fe^{2+} and Fe^{3+} species, respectively. The signal observed at 711.4 eV (highlighted by green color in Fig. 7d) refers to the presence of chemical bonding between Fe and N atoms, which further emphasized the presence of Fe–N_x species in the electrocatalyst.[41] These moieties play a vital role in boosting the ORR activity and durability, particularly in the acidic conditions.[55] The high ORR activity of the Fe–N_x species towards the ORR are attributed to the small cleavage barrier of the O–O bond over the Fe–N_x active sites, preferable interaction between Fe–N_x and the ORR intermediates, and the smooth electron transfer from the Fe–N_x centers to the adsorbed intermediates. Since no iron oxides peaks were detected in the XRD, the presence of Fe^{2+} and Fe^{3+} should arise from the bonding of N or S with Fe atoms, giving rise to the construction of both FeN_x and FeS_x efficient active sites in the electrocatalyst framework, which boost the ORR efficiency. Specifically, the peaks corresponding to the Fe ($2p_{3/2}$) and Fe ($2p_{1/2}$) orbitals located at binding energies of 710.1 and 720.7 eV are attributed to the Fe^{2+} bonded to sulfur, i.e., Fe–S_x.[53] Fig. S13† displays the deconvolution of the Fe 2p spectrum for the electrocatalysts obtained using 16 and 40 wt% of thiourea. Table S6† shows the proportions of the various Fe bond configurations in the synthesized electrocatalysts. The C/O ratios for the materials fabricated using thiourea, DBDS, and $Na_2S_2O_3$ were 13.72, 8.58, and 7.95, respectively, suggesting that the electrocatalyst constructed from thiourea had the best surface graphitization among all the electrocatalysts, which is vital for the fast charge transfer and reinforcing the corrosion resistance. The XPS analysis evidenced the existence of abundant active sites for catalyzing the ORR throughout the electrocatalyst carbon framework, such as pyridinic–N, graphitic–N, Fe–N_x, Fe_3C, Fe–S_x, C–S–C, and C–SO_x–C. These results reveal the synergistic effect of the dual doping of N and S in creating plentiful active sites for catalyzing the ORR. This high density of multiple active sites is the primary factor responsible for the remarkable catalytic activity of Fe–N–C/Fe_3C/C–S–C nanohybrid for ORR, whereas the significant mesoporosity plays a vital role in exposing these active sites to the electrolyte by allowing all of them to contribute in the ORR. Besides, it promotes the mass transfer process, while the high graphitization degree boost the electron transfer during the ORR electrocatalysis. To further prove the existence of Fe–N–C bonding configuration, the extended X-ray absorption fine structure (EXAFS) analysis on the Fe K-edge was done. Fig. S14† shows the Fourier-Transform (FT) plot of the EXAFS spectra of as-synthesized electrocatalyst. The FT-EXAFS data revealed that the Fe–N–C/Fe_3C/C–S–C nanohybrid displayed a notable peak at 1.50 Å, which is similar to the Fe–N bonding environment of iron phthalocyanine. This result further confirms that Fe–N–C bonding configuration is really existing in our electrocatalyst,[48,56,57] in agreement with the XPS outcomes. The additional peaks at 1.90 and 2.85 Å are attributed to the Fe-S and Fe-C bond distances, which further emphasize the existence of FeS_x and Fe_3C.[57]

2.2. Electrochemical Evaluation

View Article Online
DOI: 10.1039/D0TA06987F

The electrochemical properties of the as-synthesized electrocatalysts and the benchmark commercial Pt/C (20 wt%) as a reference material were first probed under the alkaline conditions by cyclic voltammetry (CV) and linear sweep voltammetry (LSV) in 0.10 M KOH. Fig. 8a shows the CV plots of the optimized Fe–N–C/Fe_3C/C–S–C nanohybrid, and Figs. S15† and S16† show the CV curves for the benchmark Pt/C (20 wt%) and the materials fabricated from different S precursors. All the fabricated materials exhibited pronounced cathodic peaks in O_2–saturated KOH electrolyte, whereas no reduction peaks were noticed in N_2–saturated electrolyte, suggesting the electrocatalytic response for the ORR. Fig. S17† presents the potentials at which the reduction peaks were achieved by the miscellaneous electrocatalysts. The Fe–N–C/Fe_3C/C–S–C nanohybrid fabricated using thiourea displayed the highest positive reduction peak potential (E_{red}) (0.892 V vs. RHE) among all the synthesized materials, which is even higher than that of the state-of-the-art Pt/C (20 wt%) (0.855 V vs. RHE) by 37 mV. Furthermore, it presented the largest capacitance currents in both N_2– and O_2–saturated electrolytes (Fig. S16a†), signifying that it possessed the highest electrochemical accessible surface area, which greatly strengthens the mass transfer process throughout the catalyst layers, and enhances the exposure of the active sites to the reactants, thus promoting the ORR process. This partially signifies that the electrocatalyst produced from thiourea possessed better ORR activity than the other electrocatalysts and Pt/C (20 wt%). The materials prepared from inorganic sources showed low values of E_{red} (0.751 and 0.731 V for Na_2S and $Na_2S_2O_3$, respectively). Fig. S18† shows the CV plots of the materials synthesized using different proportions of thiourea, and Fig. S19† illustrates the relation between the weight ratio of thiourea and E_{red}. It is obvious that incorporating S into the electrocatalyst substructure at a specific level resulted in improving the E_{red} from 0.834 to 0.892 V. While the use of 40 wt% of thiourea caused the E_{red} to decrease; however, it is still better than that of the electrocatalyst prepared without S-doping. The use of higher proportions of thiourea worsened the E_{red}, indicating the diminishment in the ORR performance.

To further assess the ORR performance, the LSVs curves of the different catalysts were recorded using the rotating disk electrode (RDE) under 1600 rpm (Fig. 8b). The values of the E_0, $E_{1/2}$, and J_L were extracted from the LSVs curves, and are summarized in Fig. 8c (E_0 and $E_{1/2}$) and Fig. S20† (J_L) to clearly show the influence of S precursor on the ORR activity. In this work, the values of E_0 were calculated at the current density that exceeds the threshold value of 0.1 mA cm^{-2}.[58] The materials produced from inorganic sources displayed weak ORR activities with very high overpotentials and could not attain a plateau at high current density domains. The values of E_0, $E_{1/2}$, and J_L were 0.975 V, 0.745 V, and –5.805 mA cm^{-2} for Na_2S, and 0.906 V, 0.733 V, and –5.224 mA cm^{-2} for $Na_2S_2O_3$, respectively. Based on the aforementioned physical characterizations, the inferior ORR for those samples can be attributed to NPs agglomeration, small BET SSA, low porosity, and low N content. These factors contribute to lessening the number of active centers and inhibiting the mass transfer, thus suppressing the ORR performance. On the other hand, utilizing organic feedstocks led to much enhancement in the ORR performance, where the electrocatalysts displayed rapid kinetics and achieved plateaus at low and high current density domains, consecutively. The use of DBDS improved the catalytic activity to become comparable with the commercial Pt/C (20 wt%). The electrocatalyst constructed from thiourea manifested exceptional ORR efficiency, which is even superior to the benchmark Pt/C (20 wt%), where it showed fascinating values of E_0, $E_{1/2}$, and J_L of 1.078 V, 0.929 V, and –7.218 mA cm^{-2} compared to 1.034 V, 0.889 V, and –6.451 mA cm^{-2} for the state-of-the-art Pt/C (20 wt%). The achieved ORR performance makes the Fe–N–C/Fe_3C/C–S–C nanohybrid amongst the best nonprecious ORR electrocatalysts reported to date under the alkaline conditions (Table S7†). The excellent ORR performance of the Fe–N–C/Fe_3C/C–S–C electrocatalytic system could be ascribed to the synergistic influences of many factors related to its composition and infrastructure such as: (i) The well-defined mesoporous/microporous nanostructure facilitates the accessibility of the reaction species (O_2, H_2O or H^+) to the active sites, hence promoting the mass transfer. (ii) The high BET SSA and total pore volume enhance the exposure of more active sites to the reactants, resulting in perfect exploitation of the electrocatalyst. (iii) The efficient tri-doping of N, S, and Fe heteroatoms into electrocatalyst carbon substructure resulted in breaking the electroneutrality of the carbon framework, therefore facilitating the adsorption of O_2 and enervating the O–O bonding. Moreover, high numbers of the efficient active sites were generated and uniformly distributed throughout the electrocatalyst infrastructure, such as FeN_x, FeS_x, Fe_3C, pyridinic–N, graphitic–N, C–S–C, and C–SO_x–C. This effectively elevates the density of active centers for catalyzing the ORR, hence boosting the ORR. (iv) The high graphitization degree promotes the electron transport and corrosion resistance, and prevented the dissolution of the active sites. (v) The high N doping level (6.47 at%) efficiently contributed to increasing the density of N-based active sites. (vi) The graphitic shells encapsulating the Fe_3C NPs assist their homogenous distribution, and protected them from agglomeration or dissolution during the harsh and prolonged wok conditions.

View Article Online
DOI: 10.1039/D0TA06987F

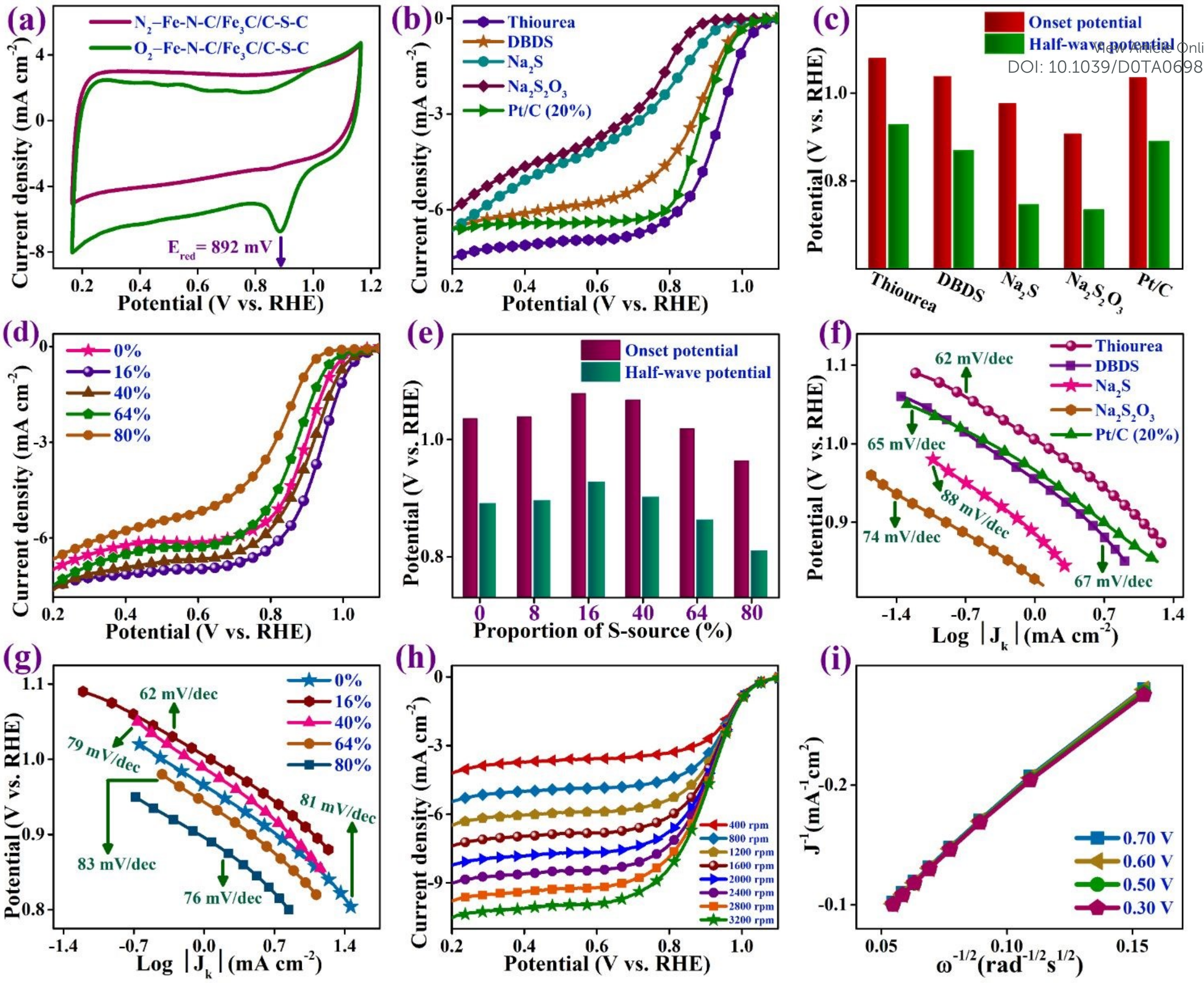

Fig. 8 (a) CV curves of the optimized Fe–N–C/Fe_3C/C–S–C nanohybrid in N_2– and O_2–saturated 0.10 M KOH solution at scan rate of 50 mV s^{-1}. (b and d) LSV curves of Pt/C (20 wt%) and Fe–N–C/Fe_3C/C–S–C electrocatalysts synthesized using different S precursors (b), and various proportions of thiourea (d), in O_2–saturated 0.10 M KOH electrolyte at scan rate of 5 mV s^{-1} and electrode rotation rate of 1600 rpm. (c) Relation between the S precursor and onset potential/half-wave potential. (e) Relation between the proportion of thiourea and onset potential/half-wave potential. (f and g) Tafel plots of Pt/C (20 wt%) and Fe–N–C/Fe_3C/C–S–C nanohybrids prepared using different S precursors (f), and various ratios of thiourea (g). (h) LSV plots of the optimized Fe–N–C/Fe_3C/C–S–C nanohybrid at different electrode rotation speeds, in O_2–saturated 0.10 M KOH electrolyte at scan rate of 5 mV s^{-1}. (i) Corresponding K–L plots at various potentials.

Fig. 8d shows the LSV plots of the electrocatalysts fabricated using different proportions of thiourea (0–80 wt%). The values of E_0, $E_{1/2}$, and J_L, were calculated from the LSV curves, and are summarized in Fig. 8e (E_0 and $E_{1/2}$) and Fig. S24† (J_L). The electrocatalyst prepared in the absence of S-doping showed E_0, $E_{1/2}$, and J_L values of 1.035 V, 0.890 V, and –6.521 mA cm^{-2}, respectively

(Fig. S21†). Utilizing small ratios of thiourea, such 8 wt%, led to a slight enhancement in the ORR catalytic activity (Fig. S22†). Further increase to 16 wt% resulted in much improvement in the E_0, $E_{1/2}$, and J_L, (Fig. 8d) implying the promotion of the ORR performance. Using 40 wt% of thiourea slightly suppressed the ORR activity; however, the performance of this sample was still superior to that of the sample synthesized without incorporating S. The materials prepared with 64 and 80 wt% showed very weak ORR catalytic activity, which was even inferior to the material fabricated without S-doping. The deterioration of the ORR performance on using high proportions of thiourea is mainly due to the diminution in the BET SSA and porosity, as well as the NPs agglomeration, which led to decreasing the number of active sites and inhibiting the mass transfer process. These results demonstrate that adjusting the S-doping level into the carbon skeleton is of utmost significance for maximizing the ORR electrocatalysis. To get insights about the catalytic contribution of Fe-based active sites in promoting the ORR efficiency, another sample was prepared without adding the Fe precursor. The LSV curve of this sample showed that this sample displayed very low ORR activity as indicated from the low values of E_0 and $E_{1/2}$ (0.792 and 0.653 V, respectively), comparing to 1.078 and 0.929 V for the sample prepared in the presence of Fe precursor (Fig. S23†). The drop in the ORR performance in the Fe-free catalyst is due to the absence of Fe-based active sites like Fe_3C NPS and Fe–N_x species, which have excellent activity for catalyzing the ORR process. These results demonstrate that Fe_3C NPS and Fe–N_x species have a predominant role in enhancing the electrocatalytic activity of Fe–N–C/Fe_3C/C–S–C nanohybrid. It can be concluded that the multi-doping of N and S as well as Fe into the carbon framework at an ideal level is vital for maximizing the ORR performance, due to the redistribution of the spin and charge densities of the carbon skeleton and the increment in the density of active sites, whose synergistic effects tremendously reinforce the ORR electrocatalysis. Besides; adjusting the ratios of the precursors is of extreme importance, where it has dramatic influences on the efficiency of the heteroatom-doping level, BET SSA, porosity, and graphitization degree of the electrocatalyst. All of those parameters are key issues for improving the ORR efficiency.

In the LSV voltammograms of the ORR, there are two zones of concern for investigation, which are the kinetic-controlled zone at low current densities, and the diffusion-controlled zone at high current densities. The kinetic-controlled regions for the materials fabricated from different S precursors were examined by plotting Tafel curves derived from the LSV polarizations curves at low overpotentials and rotation speed of 1600 rpm (Fig. 8f). The nanomaterials synthesized from organic S sources showed smaller Tafel slopes (62 and 67 mV dec^{-1}, for thiourea and DBDS) than those obtained from inorganic ones (74 and 88 mV dec^{-1}, for $Na_2S_2O_3$ and Na_2S). The small Tafel slope (62 mV dec^{-1}), which is slightly smaller than that of the commercial Pt/C (65 mV dec^{-1}), suggests that the as-fabricated Fe–N–C/Fe_3C/C–S–C nanohybrid has fast ORR kinetics analogous to Pt/C (20 wt%), and the first electron transfer is perhaps the rate-determining step for the ORR process on both electrocatalysts.[14] The rapid ORR kinetics enhance the ORR performance. Fig. 8g displays the Tafel plots for the electrocatalysts prepared with various proportions of thiourea. The electrocatalyst obtained without S-doping showed high Tafel slope (81 mV dec^{-1}), indicating the sluggish ORR kinetics occurring on that electrocatalyst. When a small weight percentage of thiourea, such as 16 wt%, was employed to incorporate S into the electrocatalyst framework, the Tafel slope decreased to 62 mV dec^{-1}, suggesting the enhancement of the ORR kinetic process. Using high percentages of thiourea led to increasing the Tafel slope to values between 76 and 83 mV dec^{-1}. To attain deep insights into the ORR catalyzed by Fe–N–C/Fe_3C/C–S–C nanohybrid, we measured the ORR polarization curves at multiple rotation speeds (400-3200 rpm), as shown in Fig. 8h. It is obvious that the current density in the RDE voltammograms was enhanced with increasing the RDE rotation speed, because of promoting the oxygen flow on the electrode surface, as a result of shortening the diffusion distance at high rotation velocities. The diffusion-controlled behavior of Fe–N–C/Fe_3C/C–S–C nanohybrid was scrutinized by plotting the Koutecky–Levich (K–L) curves, which were extracted from the LSV curves under various rotation speeds (Fig. 8i). The excellent linearity of the K–L plots reveals that the ORR on Fe–N–C/Fe_3C/C–S–C follows a first-order reaction kinetics with respect to the concentration of the dissolved O_2 in the electrolyte. The perfect parallelism and overlapping indicate identical ORR electron transfer number (n), regardless of the potential. Since the K–L plots are nearly coincident, they displayed the same slope, and hence the calculated n values were found to be the same at various potentials (0.30 – 0.70 V). The n was determined to be 4.03, divulging the high selectivity towards the direct four-electron transfer pathway in the alkaline environment ($O_2 + 2H_2O + 4e^- \rightarrow 4OH^-$), without the formation of any obnoxious intermediates. Fig. S25† shows the linear fitting plot for the K–L curve obtained at 0.60 V. We also recorded the ORR polarization curves under different RDE rotating rates for the commercial Pt/C (20 wt%) as a reference catalyst (Fig. S26a†), and the corresponding K–L plots are shown in Fig. S26b†. The calculated n based on the K–L equation was 3.98. Fig. S27† shows the linear fitting plot for the K–L curve of Pt/C (20 wt%) obtained at 0.60 V.

The kinetic current density (J_K) is an important criterion to further assess the catalytic activity of materials**.** Fig. 9a shows the J_K values accomplished by the different electrocatalysts at a potential value of 0.90 V vs. RHE. The nanomaterials produced from organic sources achieved much better J_K than those obtained from inorganic sources. For instance, the electrocatalyst constructed from thiourea displayed the highest J_K (12.29 mA cm^{-2}) among the series, and shows 3.2-times enhancement compared to that of the benchmark Pt/C–20 wt% (3.85 mA cm^{-2}), demonstrating that the ORR kinetics are occurring faster on Fe–N–C/Fe_3C/C–S–C than on Pt/C (20 wt%) and the other prepared materials. The improved J_K is because of the high density of catalytic sites and the abundant porosity that promotes the reactants accessibility to the active sites, and hence assisting in the efficient utilization of the electrocatalyst. The weight ratio of thiourea showed great influence on the J_K of the catalysts (inset of Fig. 9a). While doping S into the electrocatalyst led to significant improvement in J_K, increasing the S-doping above a specific level led to a gradual decay in J_K. This further confirms the dominance of S in controlling the ORR behavior of the electrocatalyst.

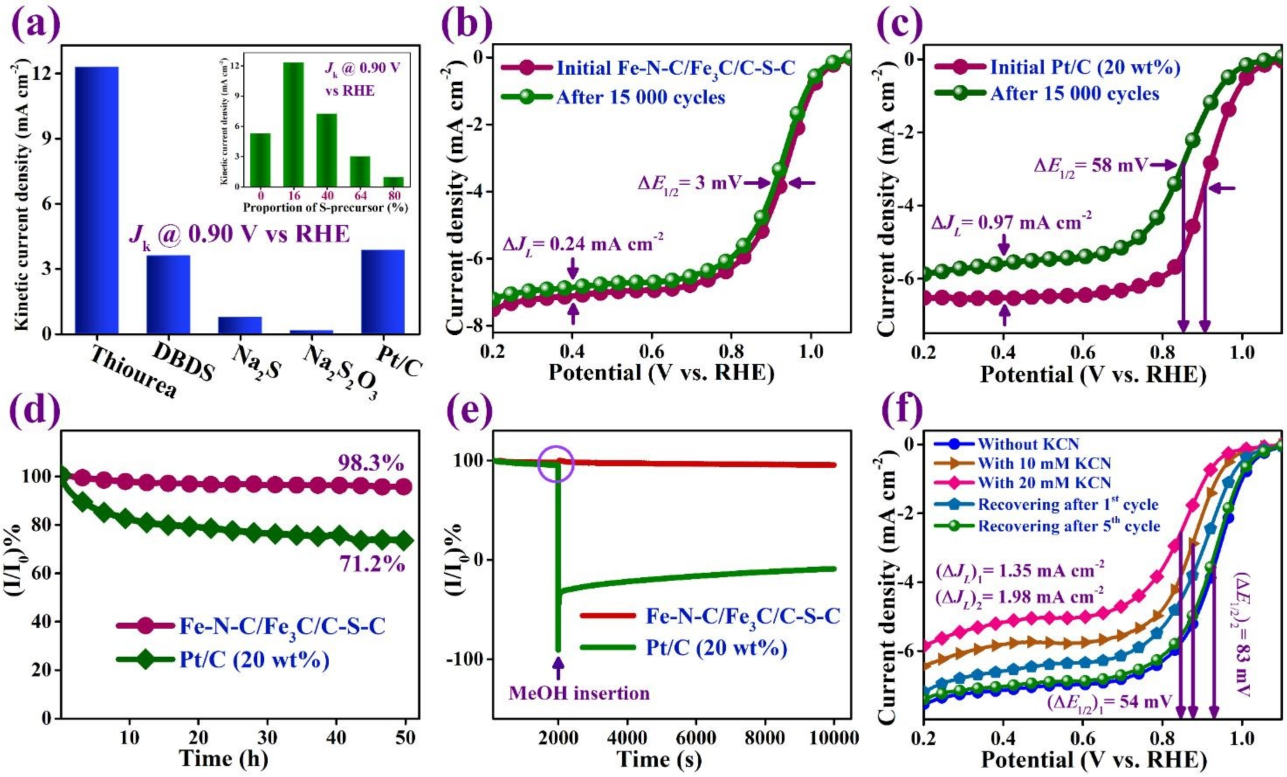

Fig. 9 (a) Comparison of kinetic current density (J_K) at potential of 0.90 V vs RHE, for the electrocatalysts fabricated using different S precursors. The inset in Fig. 8a shows the relation between J_K and the proportion of thiourea. (b and c) LSV curves of Fe–N–C/Fe$_3$C/C–S–C nanohybrid (b), and Pt/C (20 wt%) (c), before and after 15 000 potential cycles in O–saturated 0.10 M KOH electrolyte. (d) Current-time chronoamperometric curves for 50 h at 0.70 V vs RHE in O_2–saturated 0.10 M KOH, for Fe–N–C/Fe$_3$C/C–S–C nanohybrid and commercial Pt/C (20 wt%). (e) Methanol-tolerance evaluation of Fe–N–C/Fe$_3$C/C–S–C and Pt/C (20 wt%) examined by the chronoamperometric response, where CH_3OH was injected after 2000 s into the O_2–saturated 0.10 M KOH electrolyte. (f) Effect of the CN^- ions on the ORR activity of Fe–N–C/Fe$_3$C/C–S–C nanohybrid, in O_2–saturated 0.10 M KOH electrolyte at scan rate of 5 mV s^{-1} and electrode rotation speed of 1600 rpm.

The active cathode electrocatalyst should retain outstanding performance along with durability to be able to survive in the fuel cell experimentation and working conditions. An accelerated durability test (ADT) has been performed to comprehend how the electrocatalyst survives under severe working environment. The ATD was implemented by the potential cycling between 0.4 and 1.1 V vs RHE in O_2–saturated 0.10 M KOH for 15,000 cycles at a sweep rate of 100 mV s^{-1}. The extent of deterioration in performance was estimated from the shifts in $E_{1/2}$ and J_L. The LSVs curves of the Fe–N–C/Fe$_3$C/C–S–C nanohybrid recorded before and after the ADT (Fig. 9b) showed that the losses in $E_{1/2}$ and J_L were only 3 mV and 0.24 mA cm^{-2}, consecutively. On the other hand, the Pt/C (20 wt%) counterpart displayed severe degradation in the ORR performance, where the losses in $E_{1/2}$ and J_L were 58 mV and 0.97 mA cm^{-2}, respectively (Fig. 9c). The ADT results obviously reveal that our electrocatalyst possesses extraordinary stability under the stimulated harsh electrochemical conditions in the alkaline electrolyte compared to the state-of-the-art Pt/C (20 wt%). The excellent durability of Fe–N–C/Fe$_3$C/C–S–C nanohybrid is due to the stable Fe–N$_x$ coordination incorporated into electrocatalyst carbon framework, and the efficient protection of the Fe-based NPs by the NS-doped graphitic shells, which prohibit the NPs from dissolution, sintering, and agglomeration. Besides, the sufficient degree of carbon graphitization boosts the durability of the carbon matrix against corrosion during the long-time operation, hence safeguarding the active sites from disintegration. As a result, the Fe–N–C/Fe$_3$C/C–S–C nanohybrid maintained its superb performance for prolonged period, even under harsh operating conditions. The drop in the activity of the Pt/C (20 wt%) might be because of the dissolution accompanied with coalescing of Pt NPs during the potential cycling.[59]

I–t approach at 1600 rpm for 50 h was utilized to further corroborate the magnificent electrochemical stability of Fe–N–C/Fe$_3$C/C–S–C nanohybrid (Fig. 9d). After 50 h of continuous operation, our electrocatalyst displayed a slight decay of 1.7% in the current density, whereas the benchmark Pt/C (20 wt%) suffered from remarkable deterioration of 28.8% in the current density under the same working conditions. The nanostructure of Fe–N–C/Fe$_3$C/C–S–C electrocatalyst after the stability test has been investigated by TEM and HRTEM at various positions (Fig. S28†). It is clear that there were almost no alterations in the electrocatalyst morphology after the long-term durability test. Furthermore, the Fe-based NPs could be distinctly discerned, and no agglomeration happened, even after 15,000 potential cycles. In addition, the graphitic domains are still clearly seen, suggesting that the electrocatalyst carbon infrastructure is extremely resistant to corrosion, which is essential for protecting the active cites from leaching out, and the porosity from collapsing. Since the electrocatalyst maintained its structure after 15,000 CV cycles, it is rational to attribute the superb durability to the maintenance of the structural and chemical composition. These outcomes emphasize that the Fe–N–C/Fe$_3$C/C–S–C nanohybrid outperforms the state-of-the-art commercial Pt/C (20 wt%), in terms of electrocatalytic activity, selectivity, and durability. The resistance to methanol (CH_3OH) is of great importance for the electrocatalyst applicability in direct methanol fuel cells. Chronoamperometric measurements (*I–t*) for 10,000 s were performed to check the sensitivity of Fe–N–C/Fe$_3$C/C–S–C nanohybrid to CH_3OH (Fig. 9e). When 5 mL of CH_3OH (5 M) were injected, after 2000 s, into the test cell containing O_2–saturated 0.10 M KOH electrolyte, our electrocatalytic system did not show any response to CH_3OH, corroborating the high selectivity of the electrocatalyst towards the ORR, and the premium resistance to CH_3OH. Conversely, the ORR current of the commercial Pt/C (20 wt%) displayed a remarkable drop, and the sign of the current was even reversed, due to the oxidation reaction of CH_3OH. After continuing the I–t measurements until 10,000 s, the ORR current of the Fe–N–C/Fe_3C/C–S–C nanohybrid maintained almost all of its initial performance (99.6% retention), confirming the excellent tolerance to CH_3OH crossover, and the possible applicability as a cathode material in direct methanol fuel cells, instead of the commercial Pt/C.

To describe the catalytic contribution of Fe–N_x sites in catalyzing the ORR, the ORR polarization curves were recorded in the presence of 10 and 20 mM KCN solution, with a continuous pumping of O_2 into the test cell. Cyanide (CN^-) anions are well known to form a stable chelate complex with Fe cations that exist in the form of Fe–N_x species in the carbon matrix;[60] therefore, they can hinder these sites from catalyzing the ORR. When 5 mL of 10 mM KCN solution were introduced into the O_2–saturated 0.10 M KOH, a significant drop in the ORR activity occurred, where the values of $E_{1/2}$ and J_L were negatively shifted by 54 mV and 1.35 mA cm^{-2}, respectively (Fig. 9f). Upon injecting more concentration of KCN solution, the ORR performance degraded more severely, as can be seen from the more negative shifts of $E_{1/2}$ and J_L (83 mV and 1.98 mA cm^{-2}), i.e., additional losses of 29 mV and 0.63 mA cm^{-2} happened when more concentration of KCN was inserted into the test cell, due to the blocking of more Fe–N_x sites by CN^- anions. When the working electrode was rinsed multiple times with ultrapure water, and retested in a fresh O_2–saturated 0.10 M KOH electrolyte, the $E_{1/2}$ and J_L shifted to more positive values after performing the first cycle, revealing that the electrocatalyst started to recover its initial performance. After the fifth cycle, the initial electrocatalytic activity was nearly regained. These results not only corroborate the existence of Fe–N_x sites within the electrocatalyst carbon matrix, in consistence with the XPS outcomes, but also emphasize the fundamental role of these active centers in promoting the ORR electrocatalysis.

Considering that the S- and Fe-free samples showed lower ORR activity as compared to the S- and Fe-doped samples, it can be concluded that: 1) The S-based species such as FeS_x, C–S–C, and C–SO_x–C have a significant role in enhancing the ORR activity of the herein synthesized electrocatalyst, where the absence of these sites resulted in weakening the ORR performance. 2) Both Fe_3C NPS and Fe–N_x moieties have a predominant role in catalyzing the ORR, where the absence of these active sites resulted in too much deterioration of the ORR activity of the catalyst. 3) Fe–N_x species have excellent activity towards the ORR, where the blocking of theses active centers resulted in a significant drop in the ORR performance. 4) the coexistence of FeN_x, FeS_x, Fe_3C, C–S–C, and C–SO_x–C species is essential for maximizing the ORR activity of electrocatalyst, where the absence of any of these species resulted in degrading the ORR performance. This emphasizes that the multi-doping of N and S as well as Fe into the carbon framework at an ideal level is vital for reaching a maximum ORR efficiency, due to the redistribution of the spin and charge densities of the carbon skeleton and the increment in the density of active sites, whose synergistic effects tremendously reinforce the ORR electrocatalysis.

The ORR catalytic activity of Fe–N–C/Fe_3C/C–S–C nanohybrid was also evaluated in the acidic environment. The electrocatalyst displayed a well-defined reduction peak at 0.763 V vs. RHE in O_2–saturated 0.10 M $HClO_4$ solution (Fig. 10a), indicating the admirable ORR activity in the acidic medium. Fig. 10b show the LSVs curves at 1600 rpm of Fe–N–C/Fe_3C/C–S–C catalytic system and the state-of-the-art Pt/C (20 wt%). It distinctly seen that the two catalysts exhibited similar E_0 values. Regarding the $E_{1/2}$ and J_L, our electrocatalyst manifested comparable performance to the commercial Pt/C (20 wt%), where it showed lower values of $E_{1/2}$ and J_L by only 24 mV and 0.46 mA cm^{-2}, consecutively. This demonstrates that our Fe–N–C/Fe_3C/C–S–C nanohybrid has efficient ORR performance under the acidic conditions as well, which is one of the best performances reported to date in the acidic electrolytes (Table S8†). The J_K values provided by Fe–N–C/Fe_3C/C–S–C and commercial Pt/C (20 wt%) electrocatalysts were 1.75 and 3.54 mA cm^{-2}, consecutively, indicating that the reaction rate was lower on the Fe–N–C/Fe_3C/C–S–C nanohybrid than on the Pt/C in the acidic electrolyte. The Fe–N–C/Fe_3C/C–S–C nanohybrid showed very similar Tafel slope to the benchmark Pt/C (20 wt%), as can be seen from Fig. 10c (73 and 71 mV dec^{-1}), revealing that similar reaction mechanisms occurred on both electrocatalysts and the transfer of the first electron during the ORR catalysis is the rate-determining step for the reaction. To further investigate the ORR mechanism on Fe–N–C/Fe_3C/C–S–C with respect to the state-of-the-art Pt/C (20 wt%), the LSV measurements were carried out at multiple rotation speeds (400-3200 rpm) for both electrocatalysts (Figs. S29a† and S31a†). It is apparent that accelerating the rotation speed of the RDE resulted in promoting the reduction current density, due to the reinforcement of the mass transport, indicating that the ORR catalysis is a kinetically-controlled process. The corresponding K–L curves are exhibited in Figs. S29b† and S31b†. The K–L plots for both electrocatalysts show admirable linearity and parallelism, disclosing a first-order ORR kinetics and similar charge transfer mechanism. The determined *n* values based on the K–L curves of Fe–N–C/Fe_3C/C–S–C and Pt/C (20 wt%) were realized to be 3.95 and 3.97, respectively, demonstrating that the ORR on the surface of both electrocatalysts happened through a single-step reaction kinetics, where the oxygen molecules were directly reduced to water ($O_2 + 4H^+ + 4e^- \rightarrow 2H_2O$). This further confirms the outstanding electrochemical performance of the Fe–N–C/Fe_3C/C–S–C nanohybrid under acidic conditions.

View Article Online
DOI: 10.1039/D0TA06987F

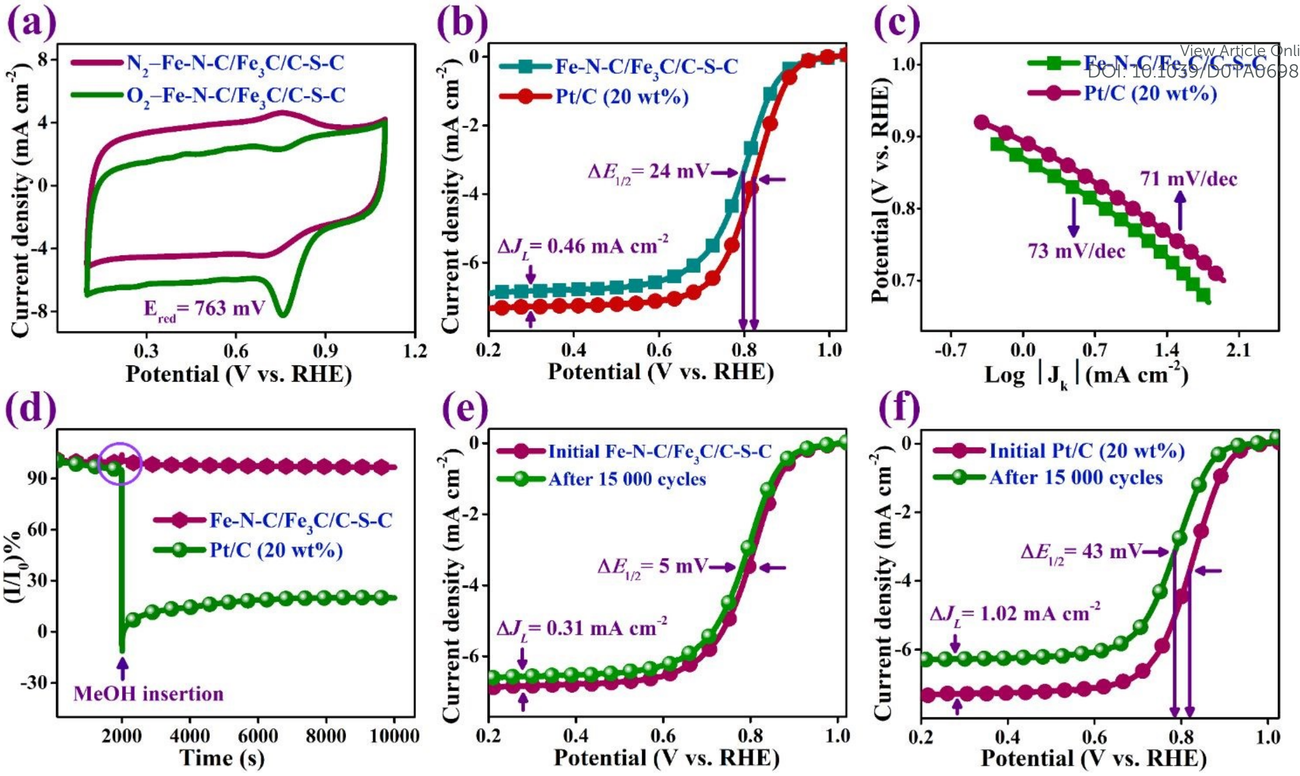

Fig. 10 (a) CV curves of Fe–N–C/Fe_3C/C–S–C nanohybrid in N_2– and O_2–saturated 0.10 M $HClO_4$ electrolyte at scan rate of 50 mV s^{-1}. (b) LSV curves of Fe–N–C/Fe_3C/C–S–C and Pt/C (20 wt%), at 1600 rpm in O_2–saturated 0.10 M $HClO_4$ electrolyte at scan rate of 5 mV s^{-1}. (c) Tafel plots of Fe–N–C/Fe_3C/C–S–C and Pt/C (20 wt%). (d) Chronoamperometric response of methanol on Fe–N–C/Fe_3C/C–S–C and Pt/C (20 wt%), at 1600 rpm upon methanol addition after 2000 s into the O_2–saturated 0.10 M $HClO_4$ electrolyte. (e and f) ORR polarization curves of Fe–N–C/Fe_3C/C–S–C nanohybrid (e), and Pt/C (20 wt%) (f), before and after 15 000 potential cycles in O_2–saturated 0.10 M $HClO_4$ electrolyte.

The CH_3OH tolerance in the acidic electrolyte was explored by the *I*–*t* measurements (Fig. 10d). Upon introducing 5 mL of CH_3OH (5 M) into the O_2–saturated 0.10 M $HClO_4$ solution, there was no alteration in the current density of the Fe–N–C/Fe_3C/C–S–C; meanwhile, there was a considerable drop in the current density of Pt/C, due to the oxidation of CH_3OH on its surface. Even after 10,000 s, our electrocatalyst did not show any susceptibility to CH_3OH, and the current preserved almost all of its initial value (with 99.1% retention), demonstrating the high durability, even in the presence of poisoning effects. In contrast, Pt/C maintained only 21.3% of the initial current, demonstrating the outperformance of the Fe–N–C/Fe_3C/C–S–C nanohybrid over the commercial Pt/C regarding the methanol tolerance. The stabilities of Fe–N–C/Fe_3C/C–S–C nanohybrid and the benchmark Pt/C (20 wt%) were assessed under the acidic conditions by performing the ADT with a continuous supply of O_2 in 0.10 M $HClO_4$ electrolyte for 15,000 CV cycles between 0.4 and 1.1 V vs. RHE at a scan rate of 100 mV s^{-1}. The extent of decay in performance was measured by recording the ORR polarization curves before and after the ADT (Fig. 10e and 10f). Our Fe–N–C/Fe_3C/C–S–C nanohybrid manifested outstanding stability, with negligible negative shifts of 5 mV and 0.31 mA cm^{-2} in $E_{1/2}$ and J_L, consecutively (Fig. 10e). In contrast, the commercial Pt/C (20 wt%) presented negative shifts of 43 mV and 1.02 mA cm^{-2} in $E_{1/2}$ and J_L, respectively, under the same operating conditions, indicating a serious decay in the ORR performance after 15,000 cycles (Fig. 10f). The marvelous durability is attributed to strong interaction between the carbon support and the active sites, efficient encapsulation of the NPs in NS-doped graphitic shells which protect the NPs from dissolution and agglomeration, and high graphitization degree which enhances the corrosion resistance of the carbon substructure, and hence safeguarding the active sites form dissolution even under harsh working environment. Based on the above results, the Fe–N–C/Fe_3C/C–S–C nanohybride can be considered a promising candidate electrocatalyst to replace the commercial Pt/C (20 wt%) in fuel cell devices and metal-air batteries, due to its excellent catalytic performance and long-term durability, high selectivity toward the ORR in the presence of CH_3OH, and efficient four-electron transfer pathway, under both acidic and basic conditions.

3. Conclusions

In summary, we report a strikingly efficient and practically applicable protocol for constructing Fe–N–C/Fe_3C/C–S–C nanohybrid. Our synthetic strategy enables the perfect encapsulation of the Fe_3C NPs into ordered mesoporous graphitic network with high specific surface area. The as-synthesized electrocatalyst showed superb ORR performance under alkaline conditions with outstanding E_0 and $E_{1/2}$ of 1.078 and 0.929 V vs RHE. In addition, it showed excellent durability after 15,000 potential cycles with zero degradation in the performance, efficient four-electron transfer pathway, and high selectivity for the ORR in the presence of methanol, under both acidic and alkaline conditions. The remarkable ORR performance of the nanohybrid is attributed the synergy of several structural merits, such as the high density of the efficient active sites (FeN_x, FeS_x, Fe_3C, pyridinic–N, graphitic–N, C–S–C, and C–SO_x–C), large surface area, well-defined micro/mesoporous substructure, high graphitization degree, unique core-shell structure, and the homogeneous distribution of the active sites throughout the electrocatalyst carbon framework. The high BET SSA enhances the exposure of the active sites to the reactants, resulting in perfect exploitation of the electrocatalyst. The well-defined mesoporous/microporous nanostructure facilitates the accessibility of the reaction species to the active sites, hence promoting the mass transfer. The high graphitization degree contributes to the efficient electron transfer during the ORR process and boosting the corrosion resistance of the carbon support. The exemplary graphitic shells proficiently enhance the electron tunneling, and protect the NPs from aggregation or dissolution under harsh operating conditions, resulting in maintaining outstanding structural durability of the interior cores, and hence strengthening the electrocatalytic stability. This pioneering protocol provides a cost-effective and sustainable approach towards the rational design of inexpensive highly active and durable ORR hybrid nanocatalysts on the large-scale production to substitute Pt-based electrocatalyst in fuel cells and metal-air batteries.

Supporting Information

Electronic Supplementary Information (ESI) available: See DOI: 10.1039/x0xx00000x

Acknowledgments

This research was supported by the Basic Science Research Program (2017R1A2B3004917) through the National Research Foundation (NRF), funded by the Ministry of Science and ICT & Future Planning of Republic of Korea.

Conflict of interest

The authors declare no conflict of interest.

References

[1] X. Yan, Y. Jia and X. Yao, *Chem. Soc. Rev.*, 2018, **47**, 7628–7658.

[2] S. Zhao, L. Yan, H. Luo, W. Mustain and H. Xu, *Nano Energy*, 2018, **47**, 172–198.

[3] A.A. Gewirth, J.A. Varnell and A.M. DiAscro, *Chem. Rev.*, 2018, **118**, 2313–2339.

[4] C. Li, H. Tan, J. Lin, X. Luo, S. Wang, J. You, Y.-M. Kang, Y. Bando, Y. Yamauchi and J. Kim, *Nano Today*, 2018, **21**, 91–105.

[5] M. Chen, Y. He, J.S. Spendelow and G. Wu, *ACS Energy Lett.*, 2019, **4**, 1619–1633.

[6] W. Xia, J. Tang, J. Li, S. Zhang, K. C.-W. Wu, J. He and Y. Yamauchi, *Angew. Chem. Int. Ed.*, 2019, **58**, 13354–13359.

[7] Y. Guo, J. Tang, J. Henzie, B. Jiang, H. Qian, Z. Wang, H. Tan, Y. Bando and Y. Yamauchi, *Mater. Horiz.*, 2017, **4**, 1171–1177.

[8] U. Martinez, S. Komini Babu, E.F. Holby, H.T. Chung, X. Yin and P. Zelenay, *Adv. Mater.*, 2019, **31**, 1970224.

[9] F. Xiao, G.-L. Xu, C.-J. Sun, M. Xu, W. Wen, Q. Wang, M. Gu, S. Zhu, Y. Li and Z. Wei, *Nano Energy*, 2019, **61**, 60–68.

[10] H. Tan, J. Tang, J. Henzie, Y. Li, X. Xu, T. Chen, Z. Wang, J. Wang, Y. Ide, Y. Bando and Y. Yamauchi, *ACS Nano*, 2018, **12**, 5674–5683.

[11] H. Tan, Y. Li, J. Kim, T. Takei, Z. Wang, X. Xu, J. Wang, Y. Bando, Y.-M. Kang, J. Tang and Y. Yamauchi, *Adv. Sci.*, 2018, **5**, 1800120.

[12] J.-C. Li, F. Xiao, H. Zhong, T. Li, M. Xu, L. Ma, M. Cheng, D. Liu, S. Feng, Q. Shi, H.-M. Cheng, C. Liu, D. Du, S.P. Beckman, X. Pan, Y. Lin and M. Shao, *ACS Catal.*, 2019, **9**, 5929–5934.

View Article Online
DOI: 10.1039/D0TA06987F

[13] Z. Guo, Z. Zhang, Z. Li, M. Dou and F. Wang, *Nano Energy*, 2019, **57**, 108–117.

[14] R. Dun, M. Hao, Y. Su, W. Li and *J. Mater. Chem. A*, 2019, **7**, 12518–12525.

[15] H. Yang, X. Chen, W.-T. Chen, Q. Wang, N.C. Cuello, A. Nafady, A.M. Al-Enizi, G.I.N. Waterhouse, G.A. Goenaga, T.A. Zawodzinski, P.E. Kruger, J.E. Clements, J. Zhang, H. Tian, S.G. Telfer and S. Ma, *ACS Nano*, 2019, **13**, 8087–8098.

[16] Y. Chen, Z. Li, Y. Zhu, D. Sun, X. Liu, L. Xu and Y. Tang, *Adv. Mater.*, 2019, **31**, 1806312.

[17] A. Zhu, L. Qiao, P. Tan, Y. Ma, W. Zeng, R. Dong, C. Ma and J. Pan, *Appl. Catal. B Environ.*, 2019, **254**, 601–611.

[18] D. Tan and F. García, *Chem. Soc. Rev.*, 2019, **48**, 2274–2292.

[19] L. Song, T. Wang, L. Li, C. Wu and J. He, *Appl. Catal. B Environ.*, 2019, **244**, 197–205.

[20] X. Ao, W. Zhang, Z. Li, J.-G. Li, L. Soule, X. Huang, W.-H. Chiang, H.M. Chen, C. Wang, M. Liu and X.C. Zeng, *ACS Nano*, 2019, **13**, 11853–11862.

[21] X. Huang, T. Shen, T. Zhang, H. Qiu, X. Gu, Z. Ali and Y. Hou, *Adv. Energy Mater.*, 2019, **9**, 1900375.

[22] R. K. Kankala, Y.-H. Han, J. Na, C.-H. Lee, Z. Sun, S.-B. Wang, T. Kimura, Y. S. Ok, Y. Yamauchi, A.-Z. Chen and K. C.-W. Wu, *Adv. Mater.*, 2020, **32**, 1907035.

[23] J. Wang, Y. Xu, B. Ding, Z. Chang, X. Zhang, Y. Yamauchi and K. C.-W. Wu, *Angew. Chem. Int. Ed.*, 2018, **57**, 2894–2898.

[24] E. Doustkhah, J. Lin, S. Rostamnia, C. Len, R. Luque, X. Luo, Y. Bando, K. C. W. Wu, J. Kim and Y. Yamauchi, *Chem. Eur. J.*, 2019, **25**, 1614–1635.

[25] J. Li, M. Chen, D.A. Cullen, S. Hwang, M. Wang, B. Li, K. Liu, S. Karakalos, M. Lucero, H. Zhang, C. Lei, H. Xu, G.E. Sterbinsky, Z. Feng, D. Su, K.L. More, G. Wang, Z. Wang and G. Wu, *Nat. Catal.*, 2018, **1**, 935–945.

[26] Q. Li, W. Chen, H. Xiao, Y. Gong, Z. Li, L. Zheng, X. Zheng, W. Yan, W.-C. Cheong, R. Shen, N. Fu, L. Gu, Z. Zhuang, C. Chen, D. Wang, Q. Peng, J. Li and Y. Li, *Adv. Mater.*, 2018, **30**, 1800588.

[27] H. Shen, E. Gracia-Espino, J. Ma, K. Zang, J. Luo, L. Wang, S. Gao, X. Mamat, G. Hu, T. Wagberg and S. Guo, *Angew. Chem. Int. Ed.*, 2017, **56**, 13800–13804.

[28] C. You, X. Jiang, L. Han, X. Wang, Q. Lin, Y. Hua, C. Wang, X. Liu and S. Liao, *J. Mater. Chem. A*, 2017, **5**, 1742–1748.

[29] T. Asefa, *Acc. Chem. Res.*, 2016, **49**, 1873–1883.

[30] J. Zhang and L. Dai, *ACS Catal.*, 2015, **5**, 7244–7253.

[31] J. Mahmood, F. Li, C. Kim, H.-J. Choi, O. Gwon, S.-M. Jung, J.-M. Seo, S.-J. Cho, Y.-W. Ju, H.Y. Jeong, G. Kim and J.-B. Baek, *Nano Energy*, 2018, **44**, 304–310.

[32] X. Xu, Z. Xia, X. Zhang, R. Sun, X. Sun, H. Li, C. Wu, J. Wang, S. Wang and G. Sun, *Appl. Catal. B Environ.*, 2019, **259**, 118042.

View Article Online
DOI: 10.1039/D0TA06987F

[33] Y. Xiong, Y. Yang, F.J. DiSalvo and H.D. Abruña, *J. Am. Chem. Soc.*, 2019, **141**, 10744–10750.

[34] D. Yan, Y. Li, J. Huo, R. Chen, L. Dai and S. Wang, *Adv. Mater.*, 2017, **29**, 1606459.

[35] A. A. Eissa, S. G. Peera, N. H. Kim and J. H. Lee, *J. Mater. Chem. A*, 2019, **7**, 16920–16936.

[36] Q. Yang, Z. Xiao, D. Kong, T. Zhang, X. Duan, S. Zhou, Y. Niu, Y. Shen, H. Sun, S. Wang and L. Zhi, *Nano Energy*, 2019, **66**, 104096.

[37] R. Saito, M. Hofmann, G. Dresselhaus, A. Jorio and M.S. Dresselhaus, *Adv. Phys.*, 2011, 60, 413–550.

[38] J.-B. Wu, M.-L. Lin, X. Cong, H.-N. Liu and P.-H. Tan, *Chem. Soc. Rev.*, 2018, **47**, 1822–1873.

[39] P. May, M. Lazzeri, P. Venezuela, F. Herziger, G. Callsen, J.S. Reparaz, A. Hoffmann, F. Mauri and J. Maultzsch, *Phys. Rev. B*, 2013, **87**, 075402.

[40] L. Bokobza, J.-L. Bruneel and M. Couzi, *C*, 2015, **1**, 77–94.

[41] Z. Tan, H. Li, Q. Feng, L. Jiang, H. Pan, Z. Huang, Q. Zhou, H. Zhou, S. Ma and Y. Kuang, *J. Mater. Chem. A*, 7 2019, **7**, 1607–1615.

[42] W.-J. Ong, L.-L. Tan, Y. H. Ng, S.-T. Yong and S.-P. Chai, *Chem. Rev.*, 2016, **116**, 7159–7329.

[43] S. Plaza, B. Mazurkiewicz and R. Gruziński, *Wear*, 1994, **174**, 209–216.

[44] A. Padamurthy, J. Nandanavanam and P. Rajagopalan, *Mater. Today Proc.*, 2019, **17**, 239–245.

[45] J. Y. Andersson and M. Azoulay, *J. Chem. Soc. Dalton Trans.*, 1986, 469–475.

[46] H. Wang, Y. Zhang, X.-L. Wu, H. Fan, Z.-Z. Luo, S. Madhavi and Q. Yan, *2D Mater.*, 2015, **2**, 035016.

[47] C. Cheng, S. Li, Y. Xia, L. Ma, C. Nie, C. Roth, A. Thomas and R. Haag, *Adv. Mater.*, 2018, **30**, 1802669.

[48] X. Fu, N. Li, B. Ren, G. Jiang, Y. Liu, F.M. Hassan, D. Su, J. Zhu, L. Yang, Z. Bai, Z.P. Cano, A. Yu and Z. Chen, *Adv. Energy Mater.*, 2019, **9**, 1803737.

[49] D. Xia, X. Yang, L. Xie, Y. Wei, W. Jiang, M. Dou, X. Li, J. Li, L. Gan and F. Kang, *Adv. Funct. Mater.*, 2019, 1906174.

[50] W.-J. Jiang, L. Gu, L. Li, Y. Zhang, X. Zhang, L.-J. Zhang, J.-Q. Wang, J.-S. Hu, Z. Wei and L.-J. Wan, *J. Am. Chem. Soc.*, 2016, **138**, 3570–3578.

[51] Z. Xia, L. An, P. Chen and D. Xia, *Adv. Energy Mater.*, 2016, **6**, 1600458.

[52] G. Li, L. Pei, Y. Wu, B. Zhu, Q. Hu, H. Yang, Q. Zhang, J. Liu and C. He, *J. Mater. Chem. A*, 2019, **7**, 11223–11233.

[53] S.N. Bhange, S.M. Unni and S. Kurungot, *ACS Appl. Energy Mater.*, 2018, **1**, 368–376.

[54] M.H. Naveen, K. Shim, M.S.A. Hossain, J.H. Kim and Y.-B. Shim, *Adv. Energy Mater.*, 2017, **7**, 1602002.

[55] S.H. Ahn, X. Yu and A. Manthiram, *Adv. Mater.*, 2017, **29**, 1606534.

View Article Online
DOI: 10.1039/D0TA06987F

[56] K. Yuan, D. Lützenkirchen-Hecht, L. Li, L. Shuai, Y. Li, R. Cao, M. Qiu, X. Zhuang, M. K. H. Leung, Y. Chen and U. Scherf, *J. Am. Chem. Soc.*, 2020, **142**, 2404–2412

[57] Y. Qiao, P. Yuan, Y. Hu, J. Zhang, S. Mu, J. Zhou, H. Li, H. Xia, J. He and Q. Xu, *Adv. Mater.*, 2018, **30**, 1804504.

[58] W. Xia, A. Mahmood, Z. Liang, R. Zou and S. Guo, Angew. Chem. Int. Ed., 2016, **55**, 2650–2676.

[59] Z. Lin, G. Waller, Y. Liu, M. Liu and C.-P. Wong, *Adv. Energy Mater.*, 2012, **2**, 884–888.

[60] H. Sun, M. Wang, X. Du, Y. Jiao, S. Liu, T. Qian, Y. Yan, C. Liu, M. Liao, Q. Zhang, L. Meng, L. Gu, J. Xiong and C. Yan, *J. Mater. Chem. A*, 2019, **7**, 20952–20957.

Rational Design of Highly Mesoporous Fe–N–C/Fe_3C/C–S–C Nanohybrid with Dense Active Sites for Superb Electrocatalysis of Oxygen Reduction

View Article Online
DOI: 10.1039/D0TA06987F

Table of Contents (TOC)

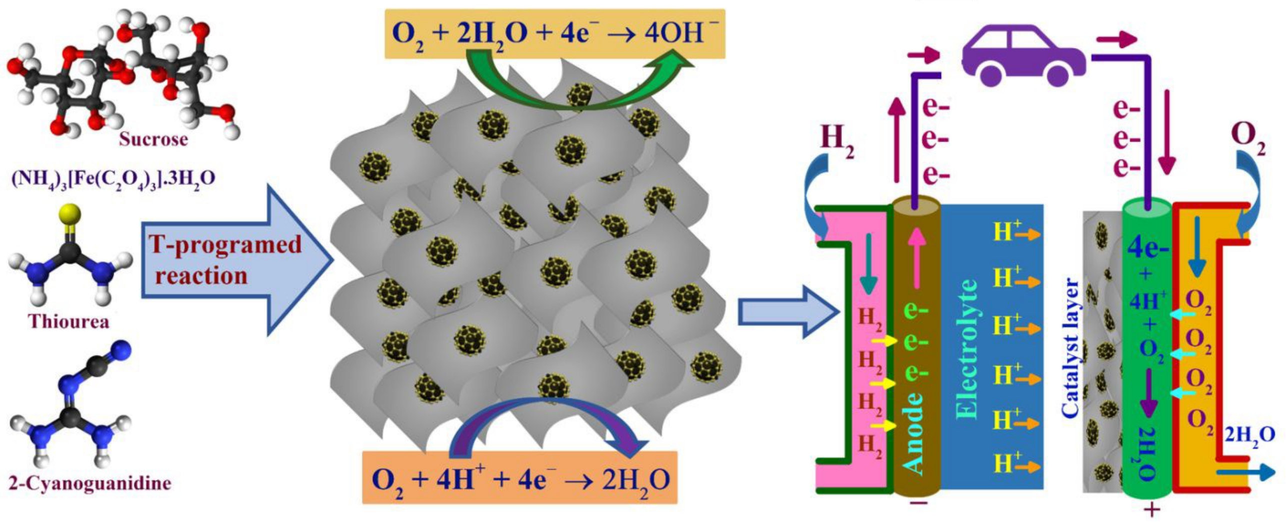

A high-performance and sustainable electrocatalyst for the oxygen reduction reaction is fabricated by a single-step doping/annealing strategy.